



HAL
open science

Interannual Coastal Trapped Waves in the Angola-Benguela Upwelling System and Benguela Niño and Niña events

Marie-Lou Bachèlery, Serena Illig, Mathieu Rouault

► To cite this version:

Marie-Lou Bachèlery, Serena Illig, Mathieu Rouault. Interannual Coastal Trapped Waves in the Angola-Benguela Upwelling System and Benguela Niño and Niña events. *Journal of Marine Systems*, 2020, 203, <10.1016/j.jmarsys.2019.103262>. <insu-03671100>

HAL Id: insu-03671100

<https://insu.hal.science/insu-03671100v1>

Submitted on 5 Aug 2025

HAL is a multi-disciplinary open access archive for the deposit and dissemination of scientific research documents, whether they are published or not. The documents may come from teaching and research institutions in France or abroad, or from public or private research centers.

L'archive ouverte pluridisciplinaire HAL, est destinée au dépôt et à la diffusion de documents scientifiques de niveau recherche, publiés ou non, émanant des établissements d'enseignement et de recherche français ou étrangers, des laboratoires publics ou privés.



Distributed under a Creative Commons CC BY 4.0 - Attribution - International License

1 **Interannual Coastal Trapped Waves in the Angola-Benguela**
2 **Upwelling System and Benguela Niño and Niña events**

3
4
5
6
7

8 Marie-Lou Bachèlery^{1,2}, Serena Illig^{3,1}, and Mathieu Rouault^{1,2}

9
10

11 ¹ Department of Oceanography, MARE Institute, LMI ICEMASA, University of Cape Town,
12 Rondebosh, South Africa.

13 ² Nansen-Tutu Centre for Marine Environmental Research, University of Cape Town,
14 Rondebosh, South Africa

15 ³ Laboratoire d'Etudes en Géophysique et Océanographie Spatiale (LEGOS),
16 CNRS/IRD/UPS/CNES, Toulouse, France

17
18

19 Re-submitted to *Journal of Marine Systems*

20 October 2019

21
22
23
24
25
26
27

28 _____

29 * Corresponding author address

30 Marie-lou Bachèlery

31 University of Cape Town (UCT), Department of Oceanography, Private Bag X3, Rondebosch
32 7701, South Africa

33 Email: bachelery.marielou@gmail.com

34 **Abstract**

35 We investigate the dynamics of the interannual Coastal Trapped Waves propagations
36 along the south-western African coast and their role in triggering Benguela Niño and Niña
37 events from 1958 to 2008. Using regional ocean model sensitivity experiments, we track
38 equatorially-forced CTW down to the Southern Benguela Upwelling System (SBUS), where
39 they account for 70% of the coastal sea level anomalies (SLA) and temperature and salinity
40 variability. We then decompose the model coastal variability into individual CTW modal
41 contributions and identify periods of energetic downwelling and upwelling propagations. A
42 composite analysis allows for documenting and quantifying the oceanic response (circulation,
43 temperature, and salinity) on the shelf during the passage of remotely-forced CTW. Results
44 reveal that North of $\sim 19^\circ\text{S}$ the coastal interannual variability is dominated by the second and
45 third CTW modes. In the BUS, their amplitudes decrease and the interannual fluctuations are
46 largely explained ($>70\%$) by the faster and weakly-dissipative first CTW mode. This
47 dynamic explains the peculiar propagative pattern associated with SLA propagations, in
48 which equatorially-forced fluctuations in the SBUS peak before the waves imprint the
49 variability at $\sim 19^\circ\text{S}$. The impact of CTW on the temperature in the SBUS is drastically lower
50 than in the NBUS and Angolan regions. At last, we show that 71% of the extreme Benguela
51 Niño and Niña events, in the surface layer, are associated with remotely-forced CTW
52 propagations. The coherence between our CTW index and those extreme event increases
53 when detecting temperature anomalies in the sub-surface rather than at the sea surface.

54

55 **Running title**

56 Interannual Coastal Trapped Waves

57

58 **Key points:**

- 59 ● Remotely-forced Coastal trapped wave dynamics controls more than 70% of the sub-
60 surface temperature, salinity, currents interannual variability along the south-western
61 African coast.
- 62 ● Interannual equatorially-forced coastal trapped waves propagate down to the southern
63 part of the Benguela Upwelling System
- 64 ● CTW propagations are dominated by the second baroclinic mode down to the
65 northern Benguela, while the faster less dissipative first mode impacts more the
66 southern Benguela Upwelling System

67

68 1. Introduction

69 Dominated by upwelling dynamics, the near-shore ocean along the south-west coast
70 of Africa is a very productive region (Carr and Kearns, 2003; Chavez and Messié, 2009;
71 Quiñones, 2010; Lachkar and Gruber, 2012). This region comprises of three alongshore sub-
72 systems almost coinciding with the political boundaries of coastal countries (**Fig. 1a**) and
73 characterised by different ocean dynamics, physico-chemical characteristics and biota
74 (Shillington, 1998; Shillington et al., 2006; Hutchings et al., 2009; Ostrowski et al., 2009).
75 The Angolan sub-system (~5°S-17°S; **Fig. 1a**) is under the influence of relatively weak
76 surface winds (Hellerman, 1980) and the Angolan poleward alongshore surface current that
77 transports the warm equatorial waters southward (Moroshkin et al., 1970; Dias, 1983a,
78 1983b; Kopte et al., 2017). A small coastal upwelling is reported, which is supported by
79 coastal waves propagations originating from the equator (Berrit, 1976; Picaut, 1983;
80 Ostrowski et al., 2009; Kopte et al., 2017). The two others sub-systems form the Benguela
81 Upwelling System (BUS), characterised by strong prevailing equatorward alongshore wind,
82 intense upwelling dynamics and the equatorward Benguela Jet (Shannon and Nelson, 1996;
83 Shillington, 1998; Shillington et al., 2006). They are separated by the major perennial
84 upwelling cell of Lüderitz at ~27°S (Lutjeharms and Meeuwis, 1987) that has been shown to
85 create a barrier for the movement of several marine species (Agenbag and Shannon, 1988;
86 Duncombe-Rae, 2005; van der Lingen et al., 2006; Lett et al., 2007). The Northern part of the
87 BUS (NBUS - ~17°S-26°S; **Fig. 1a**) hosts a permanent upwelling (Boyer et al., 2000), while
88 in the southern part of the BUS (SBUS - ~28°S-33°S; **Fig. 1a**), the upwelling is seasonal
89 (Strub et al., 1998; Hutchings et al., 2009). In the three sub-system regions, small-scale or
90 industrial fisheries are widely developed along the shore and are critical for economic
91 security and the employment of local coastal communities (Hutchings et al., 2009; Sowman
92 and Cardoso, 2010; FAO, 2011).

93 The coastal upwelling in the three sub-systems also exhibits a high variability from
94 sub-monthly to interannual timescales that has been intensively studied based on observed
95 data and model outputs (Polo et al., 2008; Goubanova et al., 2013; Lübbecke et al., 2010;
96 Rouault, 2012; Imbol Koungue et al., 2017; Illig et al., 2018b, 2018a; Illig and Bachèlery,
97 2019). These fluctuations strongly affect the marine biodiversity (Hamukuaya et al., 1998;
98 Monteiro et al., 2008; Hutchings et al., 2009; Bachèlery et al., 2016) and the regional climate
99 (Hirst and Hastenrath, 1983; Shannon et al., 1986; Rouault et al., 2003; Lutz et al., 2015).
100 The most striking example is at interannual frequencies, with episodes during which the Sea
101 Surface Temperature (SST) remains ~2°C above or below the seasonal means for ~3-6

102 consecutive months in the Angolan and NBUS sub-systems. These extreme events are known
103 as Benguela Niños and Niñas (Shannon et al., 1986; Florenchie et al., 2003, 2004). A
104 characteristic portrayal of the SST anomalies during the 2001 Benguela Niños event in the
105 area is given in **Figure 1a**. This variability is also associated with substantial modulations of
106 nutrients supply (Bachèlery et al., 2016) and of the oxygen content (Monteiro and van der
107 Plas, 2006; Monteiro et al., 2008, 2011; Bachèlery et al., 2016) during several months, as
108 illustrated on **Figure 1b**. The extended duration of non-suitable habitat conditions (hypoxia,
109 lack of food supply) is thought to affect the marine biodiversity and the abundance of the fish
110 stocks (Woodhead et al., 1997b, 1997a, 1998; Hamukuaya et al., 1998; Gammelsrød et al.,
111 1998; Binet et al., 2001; Boyer et al., 2001; Boyer and Hampton, 2001; Monteiro et al.,
112 2008).

113 It has been shown that the coastal interannual variability in the Angolan and NBUS
114 sub-systems and the Benguela Niño and Niña events are significantly related with the
115 equatorial activity (Lübbecke et al., 2010; Bachèlery et al., 2015, 2016; Imbol Koungue et al.,
116 2017; Tchibalanga et al., 2018). The equatorial forcing is associated with the propagation of
117 eastward **Equatorial Kelvin Waves (EKW)** along the equatorial waveguide due to trade wind
118 fluctuation in the western - central part of the basin (Illig et al., 2004). Upon reaching the
119 African continent, a fraction of their energy is transmitted southward and propagates along
120 the African west coast as **Coastal Trapped Waves (CTW)**. EKW and CTW can be
121 decomposed into individual modal contributions with distinct vertical structures, phase speed,
122 and dissipation rate that depend on the ocean stratification and, specifically for CTW, on the
123 cross-shore topography (Cane and Sarachik, 1976, 1977, 1979; Huthnance, 1978; Clarke and
124 Van Gorder, 1986; Brink and Chapman, 1987). Throughout their propagations, these waves
125 induce vertical and horizontal currents fluctuations impinging on the temperature (Bachèlery
126 et al., 2015), the coastal biogeochemical conditions (oxygen, nutrient, primary production;
127 Bachèlery et al., 2016) and, so on, the fish stock (Ostrowski, 2007) along the shelf.
128 Displacements of the thermocline (nutricline, and oxycline) in sub-surface are mirrored at the
129 surface by fluctuations of the **Sea Level Anomaly (SLA)** and the SST anomalies which are
130 energetic enough to be detected from space. Over the 2000-2008 period and based on high-
131 resolution numerical experiments, Bachèlery et al. (2015, 2016) have shown that the
132 equatorial forcing contributes to ~85% of the SLA, oxygen and nitrate interannual anomalies
133 along the Angolan coast. Yet, using remote-sensed observations along with regional ocean
134 model experiments, evidence of poleward propagating interannual CTW have been only
135 found from the equatorial region down to ~20°S-25°S along the western coast of Africa in the

136 NBUS (Ostrowski et al., 2009; Lübbecke et al., 2010; Bachèlery et al., 2015; Imbol Koungue
137 et al., 2017, 2019).

138 In addition to the equatorial forcing, the local atmospheric forcing also contributes to
139 the coastal interannual variability in the Angolan, and the BUS (Polo et al., 2008; Richter et
140 al., 2010). At a regional scale, interannual wind events trigger significant variations of the
141 upwelling intensity and mesoscale features, as well as locally-forced poleward propagating
142 CTW (Clarke and Brink, 1985). Recently, Imbol Koungue et al. (2017, 2019) suggested that
143 in the Angolan and NBUS sub-systems, both remote and the local forcings act concomitantly,
144 as part of a large-scale wind pattern, to trigger Benguela Niño and Niña events. Notably, they
145 highlighted the development of zonal wind stress anomalies in the western equatorial Atlantic
146 in phase with coastal meridional wind stress fluctuations along the African coast. In the
147 SBUS, since no evidence of remotely-forced interannual CTW propagation have been
148 documented, wind fluctuations are assumed to be the dominant forcing for the coastal
149 interannual fluctuations of the oceanic properties.

150 To evaluate the contribution of the remote forcing to the sub-seasonal (2-120 days⁻¹)
151 ocean dynamics, numerous studies based their methodology on the use of the SST or the SLA
152 as a proxy for the total wave signal (Polo et al., 2008; Goubanova et al., 2013). However,
153 recent analyses (Illig et al., 2018a; Illig and Bachèlery, 2019) highlighted the importance of
154 assessing the vertical structure and the propagation characteristics (forcing, amplitude, phase
155 speed, dissipation rate, and wind projection coefficient) of individual CTW modes. This
156 allows for a better estimation of the southernmost latitude at which the CTW imprints on the
157 coastal variability and a better prediction of their impact on ocean dynamics and ecosystem
158 resources. Now, at interannual timescale, despite their significant contribution, the CTW
159 modal characteristics along the south-western African continent have never been
160 documented. The objective of this study is to describe the characteristics of the interannual
161 CTW and their impact on the coastal ocean dynamics in the Angola-Benguela upwelling
162 system, as well as on the phenology of Benguela Niño and Niña. A particular effort is
163 devoted to the documentation of the impact of equatorially-forced CTW on the SBUS. We
164 also aim at unravelling the contribution of the locally-forced CTW from the equatorially-
165 forced CTW. Given the lack of an adequate observation network in the coastal band, our
166 approach relies on the numerical experimentation with a regional ocean model. Two
167 relatively long (51 years), high-resolution simulations of the south-eastern Atlantic Ocean
168 have been carried out in order to examine the equatorially-forced CTW properties as well as
169 to disentangle the role of the equatorial ocean dynamic from the local forcing in modulating

170 the coastal interannual dynamic. To do so, we benefit from a new methodology that allows to
171 extract CTW amplitude from model outputs (Illig et al., 2018b).

172 The paper is structured as follows: Section 2 presents the methodologies and
173 introduces the regional model configuration, along with the two sensitivity experiments to the
174 interannual forcing. In the supporting information, we provide a validation of the most
175 realistic simulation. Section 3 is devoted to the analysis of the model outputs. It documents
176 the effect of the interannual equatorially-forced CTW during their journey on the continental
177 shelf ocean properties. It also presents the evaluation of the CTW characteristics (phase
178 speed, magnitude, forcing) in the south-eastern Atlantic Ocean. Finally, a discussion on the
179 phenology of Benguela Niños and Niñas in regard of extreme CTW events is proposed. The
180 main conclusions and perspectives of this work are drawn in the closing section.

181

182

183 **2. Model simulations and methods**

184 The model configuration and the methodologies used to extract the contribution of the
185 EKW in the equatorial Atlantic and CTW along the south-western African coast are detailed
186 in this section. Additional information describing the data used in this study, along with the
187 validation of the model performances are given in the supporting information (section S1 and
188 S2).

189

190 ***2.1 Monthly climatologies and interannual anomalies***

191 In order to isolate the interannual variability, we use the following methodology
192 (Mosquera-Vásquez et al., 2014; Bachèlery et al., 2015). Firstly, the time series are linearly
193 detrended over the 1958-2008 period in order to remove the significant trends that are
194 observed in the region (Monteiro et al., 2008; Rouault et al., 2007, 2009) Then, the sub-
195 seasonal variability is filtered out by computing the monthly averages and smoothing them
196 using on a 1-2-1 running weighted average. Interannual anomalies are estimated by
197 subtracting the monthly climatology which is estimated over 1958–2008 (1993-2008) for
198 model solutions (remotely-sensed observation). Finally, time series are re-interpolated onto a
199 5-day time axis using cubic splines.

200

201 ***2.2 The regional ocean model configuration***

202 The Adaptive Grid Refinement in Fortran (AGRIF) version 3.1 (Penven et al., 2006;
203 Debreu et al., 2012) of the Regional Ocean Modeling System (ROMS; Shchepetkin and

204 McWilliams, 2005) is used in this study to performed the simulations. ROMS is a three-
205 dimensional, free-surface and split explicit time stepping numerical model that solves the
206 Reynolds-averaged Navier–Stokes equations based on the hydrostatic and Boussinesq
207 assumptions. The model uses finite-difference approximations on a horizontal curvilinear
208 Arakawa C grid and vertical stretched topography-following coordinate system. The vertical
209 mixing of tracers and momentum is done using a K-profile parameterisation scheme (KPP;
210 Large et al., 1994).

211 The configuration developed for this study is similar to the one of (Bachèlery et al.,
212 2015; Illig et al., 2018b). It has been used by Illig and Bachèlery (2019) to assess the coastal
213 subseasonal dynamic. The grid covers the south-eastern Atlantic Ocean including the
214 equatorial band and the BUS, extending from 7°N to 34°S, and from 10°W to the African
215 coast (**Fig. 1a**). The horizontal resolution is 1/12°, with 37 sigma vertical levels stretched in
216 the surface layer. The model bathymetry is constructed based on the GEBCO_08 global
217 elevation database at 30 arc-second spatial resolution. The domain is initialised using SODA
218 5-day averaged outputs (Carton and Giese, 2008; *cf.*, supporting information S1) on the 3rd of
219 January 1958. Model is then spun-up for 5 years using monthly climatological oceanic lateral
220 boundaries conditions and atmospheric surface forcings (estimated over the 1958-1967
221 period), before reaching a statistical equilibrium state.

222 The control run simulation, labelled ROMS-CR, is run over 51 years from 1958 to
223 2008. Forcing prescribed at the surface and at the open lateral ocean boundaries (West and
224 South) are interannual. Temperature, salinity, sea level, and currents boundary conditions
225 come from the 5-day averages of SODA reanalysis and are integrated using a mixed
226 radiation-nudging scheme (Marchesiello et al., 2001). Bulk formulae (Kondo, 1975) are used
227 to derive the freshwater, turbulent, and momentum fluxes using daily DFS5.2 (Dussin et al.,
228 2014; *cf.* supporting information S1) surface wind, temperature, and humidity fields and
229 surface heat/water fluxes (longwave and shortwave radiations and precipitation rate). As no
230 river discharges are taken into account in our simulation, model Sea Surface Salinity (SSS) is
231 restored to the 5-day SODA SSS. 5-day averages of temperature, salinity, sea level, currents
232 and wind stress outputs are saved. The pressure field is calculated offline using the
233 Thermodynamic Equation Of SeaWater 2010 (TEOS-10) from Gibbs-SeaWater
234 Oceanographic Toolbox (McDougall et al., 2011).

235 In the supporting information S2, we quantify how the model performs as compared
236 to available *in-situ* and satellite observations. This validation exercise reveals a good
237 representation of the equatorial and coastal mean state which controls the vertical structure of

238 the equatorial and coastal waves. The interannual variability is also realistically represented
239 in both sectors. Considering the good performances of the reference simulation ROMS-CR,
240 this model configuration is used to perform a sensitivity experiment labelled ROMS-EQ, to
241 examine the impact of the equatorially-forced CTW propagations on the interannual
242 variability. Assuming some linearities, comparing both simulations will allow for
243 disentangling the contribution of the equatorially-forced CTW to the coastal interannual
244 variability along the south-west coast of Africa from the impact of the local atmospheric
245 forcing.

246

247 ***2.3 Numerical Experiment ROMS-EQ***

248 Unlike ROMS-CR, in ROMS-EQ the surface atmospheric forcings (surface wind and
249 heat/water fluxes) prescribed outside of the equatorial band (7°N - 10°S) and in the eastern
250 part of the Gulf of Guinea (7°N - 10°S / 5°E -African continent) are monthly climatologies
251 estimated over the 1958-2008 period. As a result, the interannual variability along the south-
252 western coast of Africa is only triggered by the equatorial dynamics and the internal
253 variability of the model. Note that to avoid discrepancies in the wind stress curl, we have
254 applied a gradual smoothing of the atmospheric forcing fields on a transition band of 2°
255 between the climatological forcing area and regions where the daily atmospheric forcing is
256 prescribed.

257

258 ***2.4 Equatorial Kelvin Wave (EKW) forcing***

259 The EKW forcing is quantified in the equatorial Atlantic over the 1958-2008 period
260 using SODA reanalysis following the methodology used in Illig and Bachèlery (2019) and
261 adapted from (Illig et al., 2004). The methodology consists in deriving the vertical structure
262 and phase speed of the three gravest baroclinic modes using time (seasonal and interannual)
263 and zonally slow-varying stratification. Then, pressure and zonal current interannual
264 anomalies are projected onto the baroclinic structures and subsequently onto the meridional
265 structures of the EKW, accounting explicitly for the coastal boundary near the equator in the
266 Gulf of Guinea (Cane and Sarachik, 1979; Illig et al., 2004). EKW are expressed in terms of
267 their contribution to the equatorial interannual SLA averaged within the 1°S - 1°N band.

268

269 ***2.5 Coastal Trapped Waves (CTW) contribution to the coastal variability***

270 Along the south-western African coast, energetics interannual CTW are triggered by
271 the equatorial forcing (EKW) and the alongshore wind stress fluctuations. In order to

272 decipher the impact of both forcings on the CTW dynamics as well as assess the CTW
273 characteristics (amplitude and phase speed), we decomposed the coastal variability of both
274 ROMS experiments into individual CTW modes using the methodology developed by Illig et
275 al. (2018b). First, the cross-shore CTW modal structures and phase speed (*Brink and*
276 *Chapman, 1987*) of the three gravest CTW modes are derived at each latitude along the
277 south-western African continent using ROMS-CR mean (1958-2008) coastal stratification
278 and topography. Then, ROMS-CR and ROMS-EQ CTW mode amplitude are estimated by
279 projecting interannual pressure anomalies onto these structures based on the orthonormal
280 modal structure condition (*Brink, 1989*). This methodology has shown good skills in
281 estimating sub-seasonal CTW characteristics along the coasts of south-western South-
282 America and Africa (Illig et al., 2018b, 2018a; Illig and Bachèlery, 2019). In this study, CTW
283 are expressed in terms of their contribution to coastal iSLA averaged within the 0.5°-width
284 coastal band.

285 As most of the energy projects on the three gravest CTW modes (not shown), the
286 CTW propagating signal (CTW123) is considered as the summed-up contribution of the first
287 (CTW1), the second (CTW2) and the third (CTW3) CTW modes, such as:

288

$$289 \quad CTW123 = CTW1 + CTW2 + CTW3 \quad \text{Eq. 1}$$

290

291 **2.6 CTW composite analysis**

292 In order to analyse the structure and the amplitude of the interannual anomalies over
293 the continental shelf triggered during CTW propagations, we conducted composite analyses
294 based on CTW123 (*cf.* section 2.5) events index. The methodology is the following:

295 i) First, the 1958-2008 reference CTW time series are defined as the interannual
296 anomalies of CTW123 iSLA (*cf.* **Eq. 1**) for which the decadal variability is
297 removed by subtracting the 5-year running mean. As an example, the ROMS-EQ
298 CTW123 iSLA is averaged within the coastal band comprised between 19°S and
299 21°S and displayed on **Fig. 2** (grey plain line).

300 ii) Then, energetic downwelling and upwelling CTW interannual events are defined
301 when CTW123 iSLA magnitude exceeds a given threshold. On **Fig. 2**, dashed
302 horizontal black lines delineate the ± 1.5 **ST**andard **D**eviation (**STD**) thresholds
303 (used in section 3.2) and grey shading highlights periods associated with strong
304 CTW propagations.

305 iii) The delay between the passage of a CTW and its signature on the coastal

306 circulation and water masses is taken into account before performing the
307 composites. Lags are obtained by calculating the maximum lag-correlation
308 between CTW123 and the variable of interest (temperature, SLA, currents
309 components) averaged in a 0.5° coastal fringe over the 1958-2008 period. As an
310 example, the lags between the CTW passage and temperature and vertical velocity
311 averaged over the first 200m are displayed in **Fig. 3** for the $[9^\circ\text{S}-11^\circ\text{S}]$, $[19^\circ\text{S}-$
312 $21^\circ\text{S}]$, and $[29^\circ\text{S}-31^\circ\text{S}]$ domains. Timings between coastal wave peaks and ocean
313 variability will be further discussed in **section 3.4**. The red line on **Fig.2**
314 exemplifies the coastal temperature time series averaged within $[19^\circ\text{S}-21^\circ\text{S}]$ on
315 which the strong CTW propagations have been reported and overlaid with a black
316 line.

317 iv) The composite is then estimated by averaging the interannual anomalies of the
318 variable of interest during the periods of strong CTW propagations. Note that the
319 decadal variability is primarily filtered out by subtracting the 5-year running
320 mean. Assuming a symmetry between the positive (downwelling) and negative
321 (upwelling) phase of CTW (Florenchie et al., 2004; Bachèlery et al., 2015; Imbol
322 Koungue et al., 2017), interannual anomalies associated with downwelling and
323 upwelling CTW are thus combined together following the methodology of Illig et
324 al. (2014) and Bachèlery et al. (2016). It consists of multiplying by -1 the
325 interannual anomalies during periods of energetic upwelling CTW before
326 averaging all the events together. The obtained composite will thus represent the
327 response of the ocean associated with a strong downwelling CTW propagation.

328
329

330 **3. Results**

331 In this section, we analyse the results of the two sensitivity experiments in order to
332 quantify the contribution of the equatorially-forced CTW to the coastal interannual variability
333 in the Angola-Benguela upwelling sub-systems and attempt to track the signature of their
334 propagations along the western African coast from the equator down to the SBUS. We also
335 aim at documenting the characteristics of individual CTW modes namely, their forcing,
336 amplitude, dissipation rate, and phase speed, at interannual timescales.

337

338 ***3.1 Contribution of the equatorial dynamics to the coastal interannual variability***

339 The analysis starts with a comparison between the ROMS-EQ and ROMS-CR model

340 solutions (*cf.*, sections 2.2 and 2.3). **Figure 4a** shows the explained variance between the
 341 coastal (0.5° coastal band) interannual variability in the two sensitivity experiments, as a
 342 function of the latitude along the south-western African coast. Similar to **Eq.1** in Illig et al.
 343 (2018a), the explained variance (ExpVar) of ROMS-EQ relative to ROMS-CR is expressed
 344 in % and defined as:

$$345 \quad ExpVar = 100 \times \left(1 - \frac{VARIANCE(ROMSEQ-ROMSCR)}{VARIANCE(ROMSCR)} \right) \quad \text{Eq. 2}$$

346
 347 This diagnostic allows for quantifying the amount of the coastal interannual variations in
 348 ROMS-EQ, that are in phase and have the same magnitude than the amount of the coastal
 349 interannual variability in ROMS-CR, as opposed to the variability triggered by the local
 350 atmospheric forcing (surface wind and heat/water fluxes) and the model intrinsic non-
 351 linearities. Results show that the coastal iSLA variability induced by the equatorial dynamics
 352 in ROMS-EQ is highly coherent with the coastal iSLA fluctuations of ROMS-CR (**Fig. 4a**;
 353 turquoise line). This good coherence, however, decreases with latitude when moving
 354 southward, with explained variances along the coasts of Angola (9°S-11°S), Namibia (19°S-
 355 21°S) and South Africa (29°S-31°S) equal to ~81%, ~77% and ~70%, respectively. Contrary
 356 to the interannual SLA (iSLA), SSS (iSSS) and SST (iSST) variabilities are only partially
 357 explained by the remote forcing. North of 19°S, in the Angolan subsystem, ROMS-EQ
 358 explains less than 35% of ROMS-CR iSSS anomalies (**Fig 4a**; green dashed line). This
 359 contribution increases to ~50%-75% in the BUS. Note that ROMS-CR and ROMS-EQ SSS
 360 are restored to SODA SSS to compensate for the absence of river runoff in the simulations.
 361 The connection with the equatorial variability accounts for less than 50% of the coastal iSST
 362 variability, except in the Angola-Benguela Area (ABA: ~10°S - 20°S) where it peaks to
 363 ~60% (**Fig. 4a**; red dashed line). The ABA is the region where the thermocline breaks to the
 364 surface (Florenchie et al., 2004) and Benguela Niño/Niña events are more intense (**Fig. 1a**).

365 Previous studies have shown that the impact of CTW on sea surface temperature is
 366 due to fluctuations in the amplitude of the currents and the associated transport of water
 367 masses along the continental shelf (Florenchie et al., 2004; Rouault, 2012; Bachèlery et al.,
 368 2015; Rouault et al., 2018; Siegfried et al., 2019). However, the signature of CTW is also
 369 more pronounced below the surface near the thermocline where the mean vertical thermal
 370 gradient is maximum and where vertical shifts of isotherms induce strong temperature
 371 anomalies (Florenchie et al., 2004; Bachèlery et al., 2015). To that extend, the contribution of
 372 the equatorial forcing to the subsurface (averaged over the first 200 meters) coastal

373 temperature, salinity and currents (meridional and vertical) interannual anomalies is also
374 analysed using the same diagnostic (**Fig. 4b**). Similar to the iSLA, the sub-surface
375 temperature variability in ROMS-CR has a large fraction (>70%) explained by ROMS-EQ
376 solutions showing the substantial influence of the equatorial dynamics on the coastal
377 temperature variability in the Angolan, NBUS and SBUS subsystems (red line; **Fig. 4b**).
378 Similar results are obtained for sub-surface salinity with, nevertheless, a slightly weaker
379 percentage of explained variance ranging from 60% to 90% from the equator to the SBUS
380 (green line; **Fig. 4b**). The contribution of the equatorial forcing to the current variabilities
381 (meridional and vertical; plain and dashed blue lines on **Fig. 4b**, respectively) is not as clear
382 as on the iSLA, temperature or salinity variables. This might be partially due to the higher
383 dynamical nature of the currents that immediately respond to ocean and atmospheric
384 perturbation. The equatorial contribution is not continuous from the equator to the SBUS and
385 particularly drops down at Lüderitz (25°S-27°S) and Walvis Bay (16°S -17°S) illustrating the
386 stronger influence of local winds fluctuations on the currents in these two areas (see **section**
387 **3.5**). Nevertheless, a fair percentage of explained variance of ROMS-EQ relative to ROMS-
388 CR exists: North of 14°S, the coherence between the coastal interannual vertical current
389 anomalies in ROMS-EQ and ROMS-CR remains above ~50% (blue dashed line; **Fig. 4b**).
390 Within 5°S and 24°S, the remote forcing explains ~40% of the meridional current variability
391 (blue line; **Fig. 4b**).

392

393 *3.2 Impact of energetic remotely-forced CTW on the coastal circulation and shelf* 394 *water masses*

395 As interannual equatorially-forced CTW are identified as the main forcing accounting
396 for the coastal surface and sub-surface interannual variability (**Fig. 4**), we now document the
397 structure and the amplitude of the interannual anomalies triggered during the passage of
398 remotely-forced CTW on the coastal circulation (**Fig. 5**) and water masses (temperature and
399 salinity; **Fig. 6**) along the continental shelf. To do so, we performed a composite analysis (*cf.*
400 **section 2.6**) based on the detection of energetic remotely-forced CTW episodes using
401 ROMS-EQ sensitivity experiment outputs. In this experiment, the effects of the interannual
402 local atmospheric forcing have been removed (*cf.* **section 2.3**). Focusing on CTW123 iSLA
403 magnitude exceeding 1.5 STD, we identified and combined 41 CTW events including both
404 upwelling (23) and downwelling (18) CTW propagations. The delay between the passage of a
405 CTW and its impact on the coastal variability is taken into account and estimated thanks to a
406 lag-correlation analysis between the CTW123 iSLA and interannual temperature or currents

407 fluctuations. Examples of maximum correlation coefficients and associated time-lags are
408 presented in **Figure 3** for temperature and vertical currents and will be further discussed in
409 **section 3.4**. Please refer to **section 2.6** for complete details on the composite methodology.

410 To begin, we examine the impact of a downwelling CTW on the coastal circulation.
411 Shading in **Figure 5** shows CTW composites of cross-shore sections of the vertical (**Fig.**
412 **5abc**) and meridional currents (**Fig. 5def**) interannual anomalies, averaged in three regions
413 along the south-western African coast: [9°S-11°S], [19°S-21°S] and [29°S-31°S],
414 respectively. From the Angolan to the SBUS sub-systems, strong negative vertical and
415 meridional current anomalies occur along the continental shelf. They illustrate the decrease of
416 the coastal upwelling and of the surface equatorward jet, as well as the intensification of the
417 poleward meridional undercurrent associated with the passage of downwelling CTW. Off the
418 Angolan coast, maximum vertical (meridional) currents anomalies of $\sim -0.3 \text{ m.day}^{-1}$ (~ -0.05
419 m.s^{-1}) are located in the sub-surface between 100m and 200m depth (in the surface layer
420 above 100m depth). The more South, the more the impact of interannual CTW on the coastal
421 circulation is confined to the continental shelf in the coastal fringe. This can be attributed to
422 the change in the shape of the coastal bathymetry that controls the shape of the CTW modal
423 structures along the south-west coast of the African continent (Illig et al., 2018a). In the BUS,
424 the gentler continental slope favors nearly barotropic CTW characterised by vertical isopleths
425 over the shelf and slope (**Fig. 5c** and **Fig. 5f**), while in the presence of a steeper and deeper
426 bathymetry, CTW has baroclinic isopleths oriented offshore (**Fig. 5a** and **Fig. 5d**).
427 Superimposed onto the shading, contours show the correlation coefficient between
428 interannual currents (meridional and vertical) and CTW123 anomalies (shifted by a few days
429 according to the delay between the CTW passage and its signature on the coastal ocean
430 variability; **Fig. 3**; **section 2.6**). The linear relationship between equatorially-forced CTW and
431 the coastal circulation is further confirmed by the high correlation that exceeds 0.5 in the
432 three subsystems. Note also that, for both meridional and vertical currents, the spatial
433 structure of the interannual anomalies and the correlation pattern overlay extremely well.
434 Interestingly, while the amplitude of variability is decreasing southward, in particular when
435 reaching the BUS, the correlation remains constant or slightly increases with latitude.

436 CTW-associated anomalous meridional and vertical currents significantly affect the
437 transport of water masses through advection processes and therefore imprint the temperature
438 and salinity along the shelf. During the poleward propagation of a downwelling CTW,
439 temperature and salinity fluctuations are triggered by the stronger transport of equatorial
440 warm, salty water southward and the reduction of the cold, fresh subsurface water upward

441 (Fig. 5; Bachèlery et al. (2015). Interannual fluctuations of the tracers (temperature and
442 salinity) are in quadrature with the current anomalies (which corresponds to a delay of ~2
443 months between signals; Fig. 3).

444 The amplitude and the structure of the temperature and salinity interannual anomalies
445 associated with downwelling CTW propagations along the south-western African coast are
446 presented in Figure 6. The structure of the temperature (salinity) interannual anomalies
447 exhibit subsurface maxima near the coast in the first 80km at ~57m, ~63m and ~90m depth
448 (~141m, ~75m and ~97m depth) at [9°S-11°S], [19°S-21°S] and [29°S-31°S], respectively.
449 For both tracers, the magnitude of the anomalies remains high along the coast of Angola and
450 in the NBUS (temperature: ~1.5°C; salinity: ~0.06 PSU) but significantly decrease in the
451 SBUS (temperature ~0.6°C; salinity: ~0.03 PSU). This is most likely due to the decrease of
452 the amplitude of the vertical and meridional temperature and salinity gradients (not shown) in
453 the BUS and the dissipation of the energy of the CTW with latitude cause by bottom friction
454 (Illig et al., 2018b). During their propagations, remotely-forced CTW trigger a substantial
455 shift of the thermocline depth of ~10m, 15m and 5m in the 0.5°-width coastal band at [9°S-
456 11°S], [19°S-21°S] and [29°S-31°S], respectively. Alike Figure 5, we observe a good
457 coherence between temperature (salinity) and CTW123 interannual variations, with nearshore
458 maximum correlation coefficients of ~0.9, 0.9 and 0.7 (0.8,0.8 and 0.5) located near the coast
459 within ~140-180m depth at 9°S-11°S, 19°S-21°S and 29°S-31°S, respectively. In the BUS,
460 correlation patterns follow the slope of the continental shelf. Interestingly, except in the
461 SBUS, the correlation patterns do not coincide with the structure of the cross-shore tracers
462 interannual anomalies (Fig. 6abde). Interannual anomalies exhibit maximum values in the
463 subsurface above 100m depth, under the thermocline at the location of the maximum gradient
464 (not shown). As noted in Bachèlery et al. (2015, 2016), the oceanic response to CTW
465 propagations on temperature and biogeochemical tracers is dominated by the advection
466 processes and then, highly influenced by the mean vertical distribution of the tracers. In the
467 well stratified waters off the coast of Angola, the signature of the CTW is therefore located
468 under the mixed layer where the maximum vertical gradients are located (Fig. 6a and Fig.
469 6d), while in the well mixed BUS, most of the variations appear along the slope of the
470 continental shelf in agreement with the barotropic structure of the currents anomalies
471 triggered by CTW (Illig et al., 2018a, 2018b); Fig. 6c and Fig. 6f).

472 In summary, a substantial part of the coastal interannual variability is driven by the
473 equatorial dynamics. As shown in Figure 4ab, more than 70% of the iSLA and temperature
474 variability (within the first 200 m) is explained by the propagation of remotely-forced CTW

475 in the SBUS (34°S). This confirms and extends some of the earlier conclusions of Bachèlery
476 et al., (2015), but now for a longer period. It also provides for the first-time strong evidence
477 of the impact of the equatorial dynamics on ocean properties down to the southern tip of
478 south-Africa. If EKW and subsequent propagating poleward CTW are the dominant
479 mechanisms triggering the coastal oceanic variability along the south-western coast of Africa,
480 the associated interannual anomalies are expected to be trackable continuously from the
481 equator to the SBUS. Accordingly, the interannual anomalies at the equator should be
482 significantly correlated with the variability along the coast, allowing a lag to account for the
483 propagation time. The result of this simple diagnostics is illustrated in **Figure 7a** using iSLA
484 from AVISO altimetric observations (*cf.* supporting information S1). As expected, clear
485 propagations associated with significant correlation coefficients and positive increasing lags
486 (white dots on **Fig. 7a**) are observed down to ~12°S. South from this latitude, the maximum
487 correlation coefficient values significantly decrease and surprisingly, the associated lags start
488 to decrease with latitude toward negative values portraying a concave/banana-shaped pattern.
489 Therefore, according to the patterns presented in **Figure 7a**, coastal iSLA fluctuations in the
490 SBUS (~30°S) peak ~20 days before the fluctuations in the Gulf of Guinea at the equator.
491 The decrease of the consistency toward high latitude can be attributed to the resolution of the
492 satellite observations, the lack of data near the coast due to contamination that does not allow
493 accurate detection of the CTW propagations further poleward ((Polo et al., 2008; Goubanova
494 et al., 2013). However, we obtain similar patterns with ROMS-CR (**Fig. 7b**) and ROMS-EQ
495 (**Fig. 7c**) model solutions. To explain this pattern, we will now further investigate the
496 characteristics (amplitude and phase speed) of the equatorial forcing focussing in particular
497 on the equatorially-forced CTW using ROMS-EQ model outputs.

498

499 **3.3 Characteristics of the interannual CTW**

500 The amplitude of equatorially-forced CTW is mainly controlled by the amplitude of
501 the equatorial forcing, as well as by the frictional dissipation and the modal energy scattering
502 they experience along their propagation (due to bottom friction). First, we diagnose the
503 contribution of the interannual propagating EKW (*cf.* **section 2.4**) to the iSLA variability in
504 the Gulf of Guinea (**Fig. 8a**). Within [5°W-10°E / 1°S-1°N], the summed-up contribution of
505 the 3 gravest interannual EKW modes (EKW123) explains more than 60% of the equatorial
506 iSLA variability with a variance of ~1.4 cm² (**Fig. 8a** - grey bar). In agreement with Illig et al.
507 (2004) the equatorial iSLA is dominated by the contribution of EKW2 which explain ~33%
508 of its variability with a variance of 0.8 cm² (**Fig. 8a** - blue bar).

509 When reaching the African continent, a fraction of the eastward equatorial wave energy is
510 transmitted southward along the west African coast, and the coastal band is, then, considered
511 as an extension of the equatorial waveguide. The evolution of the interannual equatorially-
512 forced CTW activity in function of latitude along the south-western African coasts is
513 presented in **Figure 8** (top numbers in grey bars) by the variance of the ROMS-EQ CTW123
514 signal. Results reveal a decrease of the amplitude of the CTW123 variability by ~30 % (0.6
515 cm^2) from Angola (11°S -15°S) to South-Africa (28°S-32°S). However, while the CTW123
516 energy dissipates, its contribution to iSLA remains stable (~70 %) or even increases up to
517 ~83 % when reaching the SBUS (**Fig. 8g**). Nearby the equatorial band, down to 18°S, the
518 characteristics of remotely-forced CTW, remains consistent with the remote equatorial
519 forcing. From 7°S-10°S, the coastal iSLA interannual variability is dominated by the
520 contribution of the second CTW modes, with an explained variance of ~49% (not shown). A
521 little further south (11°S-15°S), the contribution of CTW2 tends to decrease, concomitantly
522 with the increase of the contribution of CTW3 (**Fig. 8c** - blue and green bars). The increasing
523 contribution of CTW3 to iSLA is most likely related to the scattering of CTW2 into CTW3
524 (Illig et al., 2018b). The higher the mode order, the more dissipative the mode is. Between
525 15°S and 20°S, the energy of CTW3 drastically decreases, and the less dissipative CTW2
526 became dominant. Similar to CTW3 and in agreement with the CTW2 frictional dissipation
527 decay, the amplitude of CTW2 starts to drop down from 19°S, and in the BUS, the remotely-
528 forced CTW1 become the most energetic process at work. CTW1 account for ~68% of the
529 coastal iSLA and ~80% of the CTW123 fluctuations in the SBUS between 28°S and 32°S
530 (**Fig. 8g** - red bar).

531 We now look at the propagation pattern of each CTW mode along the south-western
532 African coast. **Figure 9** illustrates the coherence between propagating CTW signal and the
533 coastal iSLA variability along the south-west coast of Africa using ROMS-EQ model
534 outputs. We compute the lag-correlation between CTW123 or individual CTW modes,
535 averaged within 7°S-9°S at the coast and the coastal iSLA at each latitude. We averaged the
536 interannual CTW contributions within 7°S-9°S at the coast because it corresponds to the
537 theoretical critical latitude (Clarke and Shi, 1991) at which the waves are trapped at the coast
538 (Bachèlery et al., 2015; Illig et al., 2018b). The time-lag allows showing the CTW
539 propagations delay. A positive time-lag means that the CTW signal is leading iSLA
540 anomalies.

541 First, results show propagating patterns along the south-eastern African coast that are
542 phase-shifted. For instance, near the equator at 8°S, the correlation coefficients between

543 CTW1 (CTW2) and the iSLA are maximum when the CTW signal leads (lags) by ~10 days
544 (**Fig. 9bc**).

545 This is explained by the fact that individual CTW modes propagate at different phase speeds
546 (i.e. CTW1: $5.5\text{m}\cdot\text{s}^{-1}$; CTW2: $2.3\text{m}\cdot\text{s}^{-1}$; CTW3: $1.2\text{m}\cdot\text{s}^{-1}$; theoretical phase speed from (Illig et
547 al., 2018b). The delay is further accentuated because, similar to CTW gravest EKW modes
548 also propagate faster than higher-order modes and reach the west coast of the African
549 continent first. Then, the further south, the more the delay between modes increases.

550 Results reveal clear poleward propagations of interannual CTW123 (**Fig. 9a**) along
551 the south-west coast of Africa from 0°S to 23°S with significant maximum correlation (**Fig.**
552 **9a** – white dots) associated with monotonically increasing time-lags when moving southward.
553 Further south, the maximum correlation coefficient decreases, and the associated lags are not
554 increasing with latitude. This propagating pattern resembles the banana-shaped pattern in
555 **Figure 7**. The coherence with individual CTW modes (**Fig 9bc**), reveals that along the south-
556 western coast of Africa, from 0°S to 23°S , the iSLA variability correlates best with the
557 CTW2. Alike **Figure 9a**, South of 23°S , the maximum correlation values diminish, and the
558 associated lags cease to increase linearly (**Fig. 9c**). Note that, a similar propagating pattern is
559 obtained with CTW3 but with much lower correlation values (<0.45) and only significant
560 between 12°S and 14°S (not shown). The coherence with CTW1 (along with the time-lags)
561 is, however, quasi continuously increasing with latitude poleward until it reaches a maximum
562 value of ~ 0.85 in the BUS (South of 23°S ; **Fig. 9b**). The fast weakly dissipative CTW1
563 impinged the iSLA in the SBUS before the dominant second mode reaches the Angolan and
564 NBUS sub-systems. This results in a significant correlation pattern that departs from a linear
565 path in the BUS and rather take a concave shape. The apparent timing inconsistency (**Fig. 7**
566 and **Fig. 9a**) is linked to the change in the dominant CTW mode from the second to the first,
567 south of 23°S).

568 Finally, using the results of **Figure 9**, we further evaluate the averaged phase speed of
569 each CTW mode propagations. Modal CTW propagation velocities are estimated based on
570 the slope of least-squares best-fit straight lines passing through the maximum correlations
571 (white dots in **Fig. 9bc**) at each latitude (within the latitudinal domain where their
572 contribution is dominant). Phase speeds obtained are $\sim 3.18\text{ m}\cdot\text{s}^{-1}$ and $\sim 1.55\text{ m}\cdot\text{s}^{-1}$ for CTW1
573 (from 4°S to 34°S) and CTW2 (from 4°S to 22°S), respectively. These velocities are in fair
574 agreement with theoretical phase speeds of the interannual CTW modes in the south-eastern
575 Atlantic Ocean (Illig et al., 2018b).

576

3.4 Timing of CTW on the coastal ocean variability

We now examine the timing between the passage of a CTW and its impact on the coastal currents and temperature variability using ROMS-CR outputs. Similar to **Figure 9a**, we perform a lag-correlation analysis between the interannual CTW123 activity averaged within [7°S-9°S] and the coastal (1°-width coastal band) vertical (**Fig. 10a**) and meridional (**Fig. 10b**) currents averaged in the [0-200m depth] surface layer at each latitude along the south-western African coast. Positive time-lags indicate that CTW123 leads the coastal circulation variability. During the passage of a downwelling CTW, vertical and meridional current fluctuations yield a shift in the position of the thermocline mirrored at the surface by fluctuations of the SLA. Therefore, the maximum correlation between the iSLA CTW123 index and the current fluctuations is associated with negative time-lags (**Fig. 10ab** and **Fig. 2**). The propagating pattern significantly differs from the one obtained with iSLA (**Fig. 9a**), with maximum correlations pattern (>0.5) following a straight path from the equator down to the SBUS. The latter is associated with a significant slower propagation speed of $\sim 0.8 \text{ m}\cdot\text{s}^{-1}$ (estimated within [4°S-33°S]) as compared to iSLA propagative pattern (**Fig. 9a**). The analysis of the impact of interannual CTW propagations on the 0-200m integrated coastal temperature fluctuations (**Fig. 10c**, shading) and on the iSST (**Fig. 10c**, contours) discloses an analogous linear pattern from the equator to $\sim 19^\circ\text{S}$. Maximum correlations are however higher (>0.7) and the estimated propagation speed is $1.53 \text{ m}\cdot\text{s}^{-1}$ (estimated within [4°S-17°S]). In the BUS (19°S-34°S), the alongshore coherency pattern with interannual temperature variability broadens toward larger time-lags and the propagation speed drastically slows down to $\sim 0.3 \text{ m}\cdot\text{s}^{-1}$ (estimated within [19°S-33°S]). The comparison between **Figure 9a** and **Figure 10** reveals that the propagative characteristics of the coastal waves are substantially different when analysing oceanic fields that are affected by slow advection processes, as opposed to SLA or thermocline depth interannual variations. Also, the discrepancy between these dynamics seems to depend on the region of interest, with larger differences between iSLA and iSST reported in the BUS. The latter are most likely associated with the specific dynamics and mean state in this major eastern boundary upwelling system, associated with a deeper thermocline, an intense mesoscale activity, and of particular interest is the presence of the equatorward Benguela Jet (Shannon and Nelson, 1996; Shillington, 1998; Shillington et al., 2006) that flows in opposite direction to the poleward CTW propagations. The identification of the processes at work requires more analyses that are beyond the scope of the present paper.

610

611 **3.5 Role of the local forcing in triggering interannual local CTW**

612 Even if we have shown that the local forcing is not the dominant mechanism behind
613 the coastal interannual variability, atmospheric fluctuations generate local wind-forced CTW
614 propagations. Along the south-west African coast, the alongshore wind stress contains a
615 substantial amount of energy at interannual timescales. The magnitude of the interannual
616 wind fluctuations is displayed in **Figure 11a** as a function of latitude along the coast. The
617 variance of the coastal wind stress is found to increase from North to South with lower values
618 ($0.005\text{-}0.007\text{ N}\cdot\text{m}^{-2}$) North of 12°S , in the Angolan subsystem. Also, the magnitude of the
619 interannual wind activity exhibit two clear maxima in the NBUS at Cape Frio ($\sim 18^{\circ}\text{S}$) and
620 the SBUS at Lüderitz ($\sim 26^{\circ}\text{S}$) which correspond to the two areas where the smallest
621 equatorial contribution to the coastal vertical current variability have been reported (*cf.*
622 **Section 3.1; Fig. 4**).

623 In order to quantify the fraction of the CTW variability explained by the coastal
624 winds, **Figure 11b** compares the variance of interannual CTW123 anomalies in ROMS-CR
625 and ROMS-EQ (dark and pale grey shading, respectively) in function of latitude along the
626 south-west African coast. Results show, that, from the equator to the SBUS, there is no
627 striking difference in the amount of energy of the propagating interannual CTW between the
628 two experiments. We quantify a maximum difference in variance smaller than 0.1 cm^2 which
629 represents only $\sim 5\%$ of the magnitude of the interannual ROMS-CR CTW123 anomalies.
630 Furthermore, **Figure 11c** shows the good coherence between the remotely-forced CTW123
631 relative to the ROMS-CR CTW123 (ExpVar in plain grey line) which explains, within the
632 three subsystems, more than 75% of the fluctuations. We observe a slightly stronger
633 CTW123 activity in the BUS in ROMS-CR compared to ROMS-EQ (**Fig. 11b**),
634 concomitantly with the enhance interannual variability of the coastal wind in the same region
635 (**Fig. 11a**). The response of the ocean to wind stress fluctuations is highly dependent on the
636 ocean stratification which controls how the wind forcing will projects its energy onto the
637 different CTW modes. Between 15°S - 30°S (**Fig. 11cd** in Illig et al. (2018a), where
638 interannual wind stress variability is strong (**Fig. 11a**). Illig et al. (2018a) have shown that the
639 wind projects preferentially on CTW1. In line with their study, model results show that
640 coastal wind interannual fluctuations in the BUS mainly force interannual CTW1 (**Fig. 11c** -
641 red plain and dash lines). Indeed, while the impact of local wind stress on each CTW mode
642 between 4°S and 19°S is non-significant, in the BUS (SBUS $\sim 30^{\circ}\text{S}$) it accounts for an
643 increase in the amplitude of CTW1 of $\sim 10\%$ ($\sim 20\%$). Wind-forced CTW1 variations in the
644 BUS are not expected to be in phase with remotely-forced variability and might affect the

645 timing and the coherence between the equatorial and the coastal variability. As a result, the
646 link between the equatorial variability and the iSLA in the BUS is slightly weakened when
647 analysing ROMS-CR outputs (not shown) compared to ROMS-EQ (**Fig. 9**).

648

649

650 **4. Discussion: Benguela-Angola Niño And Niña Analysis**

651 In this study, we have shown that the equatorial forcing, through the propagation of
652 remotely-forced CTW, explains a large amount of the interannual coastal variability and, in
653 particular, it controls 70% of the 0-200m integrated temperature fluctuations (**sections 3.1**
654 **and 3.2**). It is now natural to discuss the relation and phasing between energetic CTW and the
655 phenology of the Benguela Niños and Benguela Niñas. We therefore explore the coherence
656 between our CTW123 index and the occurrences of warm and cold events using the most
657 realistic experiment ROMS-CR.

658 As pointed out by Lübbecke et al. (2010), there is no consensus in the scientific
659 community on a criterion that identifies a Benguela Niño or Niña event. For instance,
660 Florenchie et al. (2004) define an anomalous event when the magnitude of the monthly iSST
661 averaged over the ABA region (10.5°S-19.5°S – 8.5°E-15.5°E) exceeds 1°C. Lübbecke et al.
662 (2010) consider major events as periods during which iSST fluctuations within ABA are
663 larger than ± 0.7 STD for at least three consecutive months. Imbol Koungue et al. (2017,
664 2019) classify Benguela Niños and Niñas based on the analysis of the surface temperature in
665 three distinct coastal domains of their interest (10°S-15°S, 15°S-19°S or 19°S-24°S). Extreme
666 (moderate) events are identified when their indexes exceed a ± 1 STD threshold for 3 (2)
667 consecutive months. The most complex definition is found in Lutz et al. (2013), with the
668 objective to connect the coastal SST variability to an equatorial index. These criteria all have
669 in common that they examine the temperature variations in the surface layer. Yet, it has been
670 shown by Florenchie et al. (2004) and Bachèlery et al. (2015) and supported by our results
671 that the maximum temperature variability is located under the mixed-layer, approximately at
672 the mean depth of the thermocline. In line with the aforementioned studies, we define here
673 and compare two criteria for classifying Benguela Niño/Niña events and investigate their
674 relationship with extreme CTW events. Both our criteria are defined when coastal (1°-width
675 coastal band) interannual temperature anomalies averaged within [10°S-20°S] remain higher
676 than ± 1 STD for at least 3 months in a row. The first criteria (CRIT-SURF) considers the
677 temperature averaged in the surface layer (within the first 20-meter depth), while the second
678 one (CRIT-SUBS) uses the temperature fluctuations below the mixed layer (averaged [within

679 50-60m] depth). This region undergoes a substantial decadal variability (Hutchings et al.,
680 2009; Moloney et al., 2013) that results in long periods of warm or cold condition, over
681 which the interannual anomalies are superimposed. To focus exclusively on the interannual
682 variations (period ~18 months; Florenchie et al., 2004; Bachèlery et al., 2015), prior to the
683 methodology described above, we removed the lower-frequency component by subtracting
684 the 5-year running mean. Therefore, the timing (start/end), duration, and amplitude of
685 identified events can differ from other studies, as discussed in Imbol Koungue et al. (2019).

686 **Figure 12a** displays the iSST time series along with the identified Benguela
687 Niño/Niña episodes (yellow and turquoise stars, respectively) based on CRIT-SURF
688 methodology. A total of 31 events (17 warm and 14 cold events) are selected over the 1958-
689 2008 periods. Most of these events have been documented in the literature, including the
690 extreme warm events in 1960-1961 (Imbol Koungue et al., 2019), 1963 (Shannon et al.,
691 1986; Lutz et al., 2013), 1984 (Shannon et al., 1986; Florenchie et al., 2003; Rouault et al.,
692 2003; Rouault, 2012), 1995 (Gammelsrød et al., 1998), 1999 (Mohrholz et al., 2001), and
693 2001 (Rouault et al., 2007) and the cold events in 1983 (Florenchie et al., 2004), 1985, 1992
694 (Imbol Koungue et al., 2019), 1997 (Florenchie et al., 2004), and 2003 (Bachèlery et al.,
695 2015). Periods of strong downwelling and upwelling CTW events (vertical yellow and
696 turquoise bars) are overlaid on **Figure 12a**. For consistency, here CTW events are considered
697 extreme when the time series of the summed-up contribution of the 3 first CTW modes to
698 coastal iSLA (CTW123) averaged within [10°S-20°S] exceeds ± 1 STD for 3 months in a
699 row. Results show that there is a good correspondence between indexes: of the 31 Benguela
700 Niño/Niña events, 18 events (10 warm (yellow-filled stars; **Fig. 12a**) and 8 cold (turquoise-
701 filled stars; **Fig. 12a**) are in phase with peaks in the CTW123 index, i.e. 59% of the events.
702 Among the 13 events that do not strictly coincide, 4 are, nevertheless, in phase with only
703 moderate CTW123 activity (defined as CTW123 exceeding ± 1 STD for 2 months).
704 Moreover, when analysing the contribution of individual CTW mode, results reveal that these
705 events are concomitant with the propagation of strong CTW3 (not shown), whose
706 contribution is counterweighted by CTW1 and CTW2. As a result, 22 (18+4) events can be
707 related to CTW propagation, which increase the detection performances to 71% of the
708 temperature events. This yet again emphasises the importance of disentangling the
709 contribution of individual CTW modes to better understand the dynamics of the extreme
710 events in the Angola-Benguela upwelling system. The same analysis but using the subsurface
711 temperature criterion (CRIT-SUBS), is presented in **Figure 12b**. Interestingly, the agreement
712 between both signals becomes stronger when considering the index in sub-surface: only 5

713 events (3 cold (1963, 1983, and 2001-2002) and 2 warm (1965 and 1977)) out of a total of 29
714 extreme events selected here are not associated with intense CTW123 episodes. This
715 represents a total of 83% of coherence (not shown) between signals. As alluded to earlier,
716 these specific 5 events are in phase with moderate CTW123 activity and in particular, strong
717 CTW3 propagations (not shown). Hence, 100% of the extreme temperature conditions below
718 the mixed layer can be related to energetic CTW propagations. This remarkable
719 correspondence (71% in surface and 100% in subsurface) confirmed the high dynamical
720 connection between CTW and extreme temperature conditions along the continental shelf.
721 Benguela Niños and Niñas are associated with fluctuations in the oxygen content of the shelf
722 water (**Fig. 1b**; Monteiro and van der Plas., 2006; Monteiro et al., 2008, 2011) and
723 significantly affect the marine ecosystem and fish resources (Binet et al., 2001; Gammelsrød
724 et al., 1998). Therefore, it is likely that extreme low-oxygen episodes along the continental
725 shelf and their ecological consequences are connected to CTW propagations. The advent of
726 satellites made it possible to document Benguela Niños and Niñas events as it provides
727 surface observations on a wide spatial and temporal coverage. However, our results suggest
728 that the understanding of the phenology of hypoxic and Benguela Niños and Niñas events,
729 can be significantly improved when also documenting and analysing the sub-surface
730 variability. This will, for instance, require the implementation of mooring monitoring on the
731 shelf where the CTW signature is substantial, similar to the PIRATA observational network
732 in the tropical Atlantic.

733 The analysis of **Figure 12** reveals some differences in the classification of the extreme
734 events between the surface and the sub-surface. In fact, 9 of the Benguela Niños and Niñas
735 events (warm: 1986, 1991, 1993, 1995, 2003, 2005; cold: 1972, 1985, 1992; yellow and
736 turquoise empty stars, respectively) only occur at the surface (**Fig.12a**), not fulfilling the
737 CRIT-SUBS criterion (**Fig. 12b**). Most of them nonetheless, coincide with moderate
738 temperature events in sub-surface (**Fig. 12b**) and moderate CTW propagations (not shown).
739 This implies that the local atmospheric forcing may enhance the amplitude of the extreme
740 temperature episodes in surface mixed layer (Florenchie et al., 2004; Lübbecke et al., 2010;
741 Richter et al., 2010; Bachèlery et al., 2015; Imbol Koungue et al., 2019). This is in line with
742 the recent study of Imbol Koungue et al. (2019) which highlights the concomitant role of
743 both, the equatorial and the local forcing, as part of a large-scale wind anomaly pattern over
744 the South Atlantic Ocean, in triggering Benguela Niños/Niñas.
745 However, our results reveal also cases where the atmospheric forcing (through CTW
746 generation, upwelling and evaporation processes) conceal the signature of the remotely-

747 forced CTW in the surface layer. This is in particular the case for the sub-surface 1965, 1981
748 warm (1961, 1977, 1984 cold) events (**Fig. 12b**) which are associated with strong CTW123
749 propagations but do not fulfil the CRIT-SURF criterion (**Fig. 12a**). For instance, a few
750 months before the development of the extreme warm 1995 event, the propagation of a strong
751 upwelling CTW occur along the south-western African coast (**Fig. 12** - blue bars), which
752 effects (uplifting of the thermocline and cold temperature anomalies) are recorded in the sub-
753 surface temperature (**Fig. 12b**). Surprisingly, in the surface layer, the temperature fluctuations
754 (**Fig. 12a**) portray a positive anomaly consistent with the 1995 Benguela Niño (Gammelsrød
755 et al., 1998). Our results therefore support the finding of Richter et al. (2010) who
756 disassociated the development of this event to the equatorial forcing. However, using
757 composites of Benguela Niño events over the 1958-2000 period, Lübbecke et al. (2010) did
758 not find stronger wind stress anomalies associated to the development of extreme event. To
759 our knowledge, only the 2016 Benguela Niño event was not predominantly connected to the
760 equatorial dynamics (Lübbecke et al., 2018) but was triggered by local mechanisms
761 associated with wind relaxation and enhanced freshwater from precipitation and river
762 discharges.

763

764

765 **5. Conclusion and perspectives**

766 The 1958-2008 coastal interannual variability in the south-eastern Atlantic Ocean is
767 studied using the solutions of two regional ocean model experiments. Our results highlight
768 the strong contribution of the equatorially-forced CTW to the coastal variability along the
769 shelf. For the first time, we were able to track equatorially-forced CTW propagations from
770 the equator down to 34°S in the SBUS where they contribute up to 70% of the interannual
771 SLA, temperature and salinity variability. The decomposition of model coastal variability
772 into CTW contribution allow us to document the effect of energetic CTW propagations on the
773 nearshore oceanic conditions and circulation. In the BUS, interannual remotely-forced CTW
774 induce strong meridional and vertical current anomalies, maximum in the first 200m, along
775 the slope of the continental shelf consistent with the nearly barotropic CTW structures. The
776 modulation of currents in turn affects the distribution of temperature and salinity along the
777 continental shelf. The analysis of the characteristics of individual CTW modes reveals that
778 from the equator to 22°S, the coastal variability is controlled by the contribution of the slow
779 propagating and more dissipative second and third CTW modes. Southward, their
780 contribution decreases and the less dissipative CTW1 becomes dominant. As the latter travel

781 faster, its signature on the coastal variability in the SBUS take place 10 days before the
782 higher modes impinged the NBUS.

783 Then the dynamical connection between energetics of CTW and Benguela Niño/Niña
784 events are evaluated. Our results highlight the remarkably high coherence (71%) between
785 signals. This quantification reaches 100% when: (1) focussing on fluctuations under the
786 mixed layer where the temperature variability is less influenced by the local atmospheric
787 forcing and (2) disentangling the individual CTW modal contribution to the coastal
788 variability.

789 Finally, our results also suggest a low-frequency (decadal) modulation in the intensity
790 of the surface and sub-surface temperature interannual variability and the frequency of
791 occurrence of warm/cold extreme events (stars on **Fig. 12**). We denote two periods of strong
792 activity during the [~1975-1985] and [~1995-2005] decades, interspersed with periods of
793 lower interannual variations ([~1962-1970] and [~1985-1994]). These periods are
794 concomitant with changes in magnitude of the CTW activity (vertical bars). Evaluating the
795 mechanisms that control the low-frequency modulation of the coastal interannual variability
796 will be the topic of our next research efforts

797 **Acknowledgement**

798 This work was supported by the NRF SARCHI chair on “modeling ocean-atmosphere-land
799 interactions” and the Nansen Tutu Centre. Model simulations were computed using the
800 CORE supercomputers provided by the CSAG computing facility. The ROMS model
801 simulations were built using the ROMS_TOOLS package (Penven et al., 2006) version 3.1.
802 ROMS can be downloaded from <https://www.croco-ocean.org>. The authors wish to
803 acknowledge for the use of the Ferret program for analysis and graphics in this paper. Ferret
804 is a product of NOAA's Pacific Marine Environmental Laboratory (Information is available
805 at <http://ferret.pmel.noaa.gov/Ferret/>). All data used in this study (for model forcing and
806 validation: PIRATA observations, Nansen cruise, AVISO Altimetric data, GlobCurrent
807 estimations, SODA and DRAKKAR forcing products) are publicly available, and detailed
808 information are provided in the supporting information (section S1). NOAA, NASA,
809 PANGAEA, CMEMS, GlobCurrent, and Texas A&M University are thanked for
810 development and/or the distribution of these data sets.

811

812 **Competing Interests**

813 The authors declare no competing interests.

814 **Reference**

- 815 Agenbag, J.J., Shannon, L.V., 1988. A suggested physical explanation for the existence of a
816 biological boundary at 24°30'S in the Benguela system. *South Afr. J. Mar. Sci.* 6,
817 119–132. <https://doi.org/10.2989/025776188784480726>
- 818 Bachèlery, M.-L., Illig, S., Dadou, I., 2016. Forcings of nutrient, oxygen, and primary
819 production interannual variability in the southeast Atlantic Ocean. *Geophys Res Lett*
820 43, 2016GL070288. <https://doi.org/10.1002/2016GL070288>
- 821 Bachèlery, M.-L., Illig, S., Dadou, I., 2015. Interannual variability in the South-East Atlantic
822 Ocean, focusing on the Benguela Upwelling System: Remote versus local forcing. *J*
823 *Geophys Res Oceans* 121, 284–310. <https://doi.org/10.1002/2015JC011168>
- 824 Berrit, G.R., 1976. Les eaux froides côtières du Gabon à l'Angola sont-elles dues à un
825 upwelling d'Ekman ? *Cah. ORSTOM Série Océan.* 14, 273–278.
- 826 Binet, D., Gobert, B., Maloueki, L., 2001. El Niño-like warm events in the Eastern Atlantic
827 (6N, 20S) and fish availability from Congo to Angola (1964–1999). *Aquat. Living*
828 *Resour.* 14, 99–113. [https://doi.org/10.1016/S0990-7440\(01\)01105-6](https://doi.org/10.1016/S0990-7440(01)01105-6)
- 829 Boyer, D., Cole, J., Bartholomae, C., 2000. Southwestern Africa: Northern Benguela Current
830 Region. *Mar. Pollut. Bull., Seas at the Millennium: an Environmental Evaluation* 41,
831 123–140. [https://doi.org/10.1016/S0025-326X\(00\)00106-5](https://doi.org/10.1016/S0025-326X(00)00106-5)
- 832 Boyer, D.C., Boyer, H.J., Fossen, I., Kreiner, A., 2001. Changes in abundance of the northern
833 Benguela sardine stock during the decade 1990–2000, with comments on the relative
834 importance of fishing and the environment. *South Afr. J. Mar. Sci.* 23, 67–84.
835 <https://doi.org/10.2989/025776101784528854>
- 836 Boyer, D.C., Hampton, I., 2001. An overview of the living marine resources of Namibia.
837 *South Afr. J. Mar. Sci.* 23, 5–35. <https://doi.org/10.2989/025776101784528953>
- 838 Brink, K.H., Chapman, D.C., 1987. Program for computing properties of coastal-trapped
839 waves and wind-driven motions over the continental shelf and slope. Woods Hole
840 Oceanogr. Inst., Tech. Rep. WHOI-87-24.
- 841 Cane, M., Sarachik, E., 1979. Forced Baroclinic Ocean Motions .3. Linear Equatorial Basin
842 Case. *J Mar Res* 37, 355–398.
- 843 Cane, M., Sarachik, E., 1977. Forced baroclinic ocean motions. II- The linear equatorial
844 bounded case. *J Mar Res* 35.
- 845 Cane, M., Sarachik, E., 1976. Forced Baroclinic Ocean Motions .1. Linear Equatorial
846 Unbounded Case. *J Mar Res* 34, 629–665.
- 847 Carr, M.-E., Kearns, E.J., 2003. Production regimes in four Eastern Boundary Current

848 systems. *Deep Sea Res. Part II Top. Stud. Oceanogr.*, The US JGOFS Synthesis and
849 Modeling Project: Phase II 50, 3199–3221. <https://doi.org/10.1016/j.dsr2.2003.07.015>

850 Carton, J.A., Giese, B.S., 2008. A Reanalysis of Ocean Climate Using Simple Ocean Data
851 Assimilation (SODA). *Mon Wea Rev* 136, 2999–3017.
852 <https://doi.org/10.1175/2007MWR1978.1>

853 Chavez, F.P., Messié, M., 2009. A comparison of Eastern Boundary Upwelling Ecosystems.
854 *Prog. Oceanogr.*, Eastern Boundary Upwelling Ecosystems: Integrative and
855 Comparative Approaches: Integrative and comparative approaches, 2-8 June 2008, Las
856 Palmas, Gran Canaria, Spain Eastern Boundary Upwelling Ecosystems Symposium
857 83, 80–96. <https://doi.org/10.1016/j.pocean.2009.07.032>

858 Clarke, A.J., Brink, K.H., 1985. The Response of Stratified, Frictional Flow of Shelf and
859 Slope Waters to Fluctuating Large-Scale, Low-Frequency Wind Forcing. *J. Phys.*
860 *Oceanogr.* 15, 439–453. [https://doi.org/10.1175/1520-](https://doi.org/10.1175/1520-0485(1985)015<0439:TROSFF>2.0.CO;2)
861 [0485\(1985\)015<0439:TROSFF>2.0.CO;2](https://doi.org/10.1175/1520-0485(1985)015<0439:TROSFF>2.0.CO;2)

862 Clarke, A.J., Shi, C., 1991. Critical frequencies at ocean boundaries. *J Geophys Res* 96,
863 10731–10738. <https://doi.org/10.1029/91JC00933>

864 Clarke, A.J., Van Gorder, S., 1986. A Method for Estimating Wind-Driven Frictional, Time-
865 Dependent, Stratified Shelf and Slope Water Flow. *J. Phys. Oceanogr.* 16, 1013–1028.
866 [https://doi.org/10.1175/1520-0485\(1986\)016<1013:AMFEWD>2.0.CO;2](https://doi.org/10.1175/1520-0485(1986)016<1013:AMFEWD>2.0.CO;2)

867 Debreu, L., Marchesiello, P., Penven, P., Cambon, G., 2012. Two-way nesting in split-
868 explicit ocean models: Algorithms, implementation and validation. *Ocean Model.* 49–
869 50, 1–21. <https://doi.org/10.1016/j.ocemod.2012.03.003>

870 Dias, C.A., 1983a. Note on the evidence of a permanent southward flow of the upper oceanic
871 tropospheric waters off Angola at 12°S. Collection of scientific papers of the
872 International Commission for the Southeast Atlantic Fisheries. *Collect. Sci. Pap. Int.*
873 *Comm. Southeast Atl. Fish.* 10, 99–102.

874 Dias, C.A., 1983b. Preliminary report on the physical oceanography off southern Angola,
875 March and July 1971. *Collect. Sci. Pap. Int. Comm. Southeast Atl. Fish.* 10, 103–116.

876 Duncombe-Rae, C., 2005. A demonstration of the hydrographic partition of the Benguela
877 upwelling ecosystem at 26.4S. *South Afr. J. Mar. Sci.* 27, 617–628.

878 Dussin, R., Barnie, B., Brodeau, L., 2014. The making of Drakkar forcing set DFS5.

879 FAO, 2011. Fisheries & Aquaculture - The Republic of Angola [WWW Document]. URL
880 <http://www.fao.org/fishery/facp/AGO/en> (accessed 3.19.19).

881 Florenchie, P., Lutjeharms, J.R.E., Reason, C.J.C., Masson, S., Rouault, M., 2003. The

882 source of Benguela Niños in the South Atlantic Ocean. *Geophys Res Lett* 30, 1505.
883 <https://doi.org/10.1029/2003GL017172>

884 Florenchie, P., Reason, C.J.C., Lutjeharms, J.R.E., Rouault, M., Roy, C., Masson, S., 2004.
885 Evolution of Interannual Warm and Cold Events in the Southeast Atlantic Ocean. *J*
886 *Clim.* 17, 2318–2334. [https://doi.org/10.1175/1520-](https://doi.org/10.1175/1520-0442(2004)017<2318:EOIWAC>2.0.CO;2)
887 [0442\(2004\)017<2318:EOIWAC>2.0.CO;2](https://doi.org/10.1175/1520-0442(2004)017<2318:EOIWAC>2.0.CO;2)

888 Gammelsrød, T., Bartholomae, C.H., Boyer, D.C., Filipe, V.L.L., O’Toole, M.J., 1998.
889 Intrusion of warm surface water along the Angolan-Namibian coast in February–
890 March 1995: the 1995 Benguela Nino. *South Afr. J. Mar. Sci.* 19, 41–56.
891 <https://doi.org/10.2989/025776198784126719>

892 Goubanova, K., Illig, S., Machu, E., Garçon, V., Dewitte, B., 2013. SST subseasonal
893 variability in the central Benguela upwelling system as inferred from satellite
894 observations (1999–2009). *J Geophys Res Oceans* 118, 4092–4110.
895 <https://doi.org/10.1002/jgrc.20287>

896 Hamukuaya, H., O’Toole, M.J., Woodhead, P.M.J., 1998. Observations of severe hypoxia
897 and offshore displacement of Cape hake over the Namibian shelf in 1994. *South Afr.*
898 *J. Mar. Sci.* 19, 57–59. <https://doi.org/10.2989/025776198784126809>

899 Hellerman, S., 1980. CHARTS OF THE VARIABILITY OF THE WIND STRESS OVER
900 THE TROPICAL ATLANTIC, in: Siedler, G., Woods, J.D., Düing, W. (Eds.),
901 *Oceanography and Surface Layer Meteorology in the B/C Scale*. Pergamon, pp. 63–
902 75. <https://doi.org/10.1016/B978-1-4832-8366-1.50022-4>

903 Hirst, A.C., Hastenrath, S., 1983. Atmosphere-Ocean Mechanisms of Climate Anomalies in
904 the Angola-Tropical Atlantic Sector. *J Phys Ocean.* 13, 1146–1157.
905 [https://doi.org/10.1175/1520-0485\(1983\)013<1146:AOMOCA>2.0.CO;2](https://doi.org/10.1175/1520-0485(1983)013<1146:AOMOCA>2.0.CO;2)

906 Hutchings, L., van der Lingen, C.D., Shannon, L.J., Crawford, R.J.M., Verheye, H.M.S.,
907 Bartholomae, C.H., van der Plas, A.K., Louw, D., Kreiner, A., Ostrowski, M., Fidel,
908 Q., Barlow, R.G., Lamont, T., Coetzee, J., Shillington, F., Veitch, J., Currie, J.C.,
909 Monteiro, P.M.S., 2009. The Benguela Current: An ecosystem of four components.
910 *Prog. Oceanogr.*, Eastern Boundary Upwelling Ecosystems: Integrative and
911 Comparative Approaches: Integrative and comparative approaches, 2-8 June 2008, Las
912 Palmas, Gran Canaria, Spain Eastern Boundary Upwelling Ecosystems Symposium
913 83, 15–32. <https://doi.org/10.1016/j.pocean.2009.07.046>

914 Huthnance, J.M., 1978. On Coastal Trapped Waves: Analysis and Numerical Calculation by
915 Inverse Iteration. *J Phys Ocean.* 8, 74–92. [27](https://doi.org/10.1175/1520-</p>
</div>
<div data-bbox=)

0485(1978)008<0074:OCTWAA>2.0.CO;2

916
917 Illig, S., Bachèlery, M.-L., 2019. Propagation of Subseasonal Equatorially-Forced Coastal
918 Trapped Waves down to the Benguela Upwelling System. *Sci. Rep.* 9, 5306.
919 <https://doi.org/10.1038/s41598-019-41847-1>

920 Illig, S., Bachèlery, M.-L., Cadier, E., 2018a. Subseasonal Coastal-Trapped Wave
921 Propagations in the Southeastern Pacific and Atlantic Oceans: 2. Wave Characteristics
922 and Connection With the Equatorial Variability. *J. Geophys. Res. Oceans* 123, 3942–
923 3961. <https://doi.org/10.1029/2017JC013540>

924 Illig, S., Cadier, E., Bachèlery, M.-L., Kersalé, M., 2018b. Subseasonal Coastal-Trapped
925 Wave Propagations in the Southeastern Pacific and Atlantic Oceans: 1. A New
926 Approach to Estimate Wave Amplitude. *J. Geophys. Res. Oceans* 123, 3915–3941.
927 <https://doi.org/10.1029/2017JC013539>

928 Illig, S., Dewitte, B., Ayoub, N., du Penhoat, Y., Reverdin, G., De Mey, P., Bonjean, F.,
929 Lagerloef, G.S.E., 2004. Interannual long equatorial waves in the tropical Atlantic
930 from a high-resolution ocean general circulation model experiment in 1981–2000. *J*
931 *Geophys Res* 109, C02022. <https://doi.org/10.1029/2003JC001771>

932 Illig, S., Dewitte, B., Goubanova, K., Cambon, G., Boucharel, J., Monetti, F., Romero, C.,
933 Purca, S., Flores, R., 2014. Forcing mechanisms of intraseasonal SST variability off
934 central Peru in 2000–2008. *J Geophys Res Oceans* 119, 3548–3573.
935 <https://doi.org/10.1002/2013JC009779>

936 Imbol Koungue, R.A., Illig, S., Rouault, M., 2017. Role of interannual Kelvin wave
937 propagations in the equatorial Atlantic on the Angola Benguela Current system. *J.*
938 *Geophys. Res. Oceans* 122, 4685–4703. <https://doi.org/10.1002/2016JC012463>

939 Imbol Koungue, R.A., Rouault, M., Illig, S., Brandt, P., Jouanno, J., 2019. Benguela Niños
940 and Benguela Niñas in forced ocean simulation from 1958 to 2015. *J. Geophys. Res.*
941 *Oceans*.

942 Kondo, J., 1975. Air-sea bulk transfer coefficients in diabatic conditions. *Bound.-Layer*
943 *Meteorol.* 9, 91–112. <https://doi.org/10.1007/BF00232256>

944 Kopte, R., Brandt, P., Dengler, M., Tchibalanga, P.C.M., Macuéria, M., Ostrowski, M., 2017.
945 The Angola Current: Flow and hydrographic characteristics as observed at 11°S. *J.*
946 *Geophys. Res. Oceans* 122, 1177–1189. <https://doi.org/10.1002/2016JC012374>

947 Lachkar, Z., Gruber, N., 2012. A comparative study of biological production in eastern
948 boundary upwelling systems using an artificial neural network. *Biogeosciences* 9,
949 293–308. <https://doi.org/10.5194/bg-9-293-2012>

- 950 Large, W.G., McWilliams, J.C., Doney, S.C., 1994. Oceanic vertical mixing: A review and a
951 model with a nonlocal boundary layer parameterization. *Rev Geophys* 32, 363–403.
952 <https://doi.org/10.1029/94RG01872>
- 953 Lett, C., Veitch, J., Lingen, C.D. van der, Hutchings, L., 2007. Assessment of an
954 environmental barrier to transport of ichthyoplankton from the southern to the
955 northern Benguela ecosystems. *Mar Ecol Prog Ser* 347, 247–259.
956 <https://doi.org/10.3354/meps06982>
- 957 Lübbecke, J.F., Böning, C.W., Keenlyside, N.S., Xie, S.-P., 2010. On the connection between
958 Benguela and equatorial Atlantic Niños and the role of the South Atlantic
959 Anticyclone. *J Geophys Res* 115, C09015. <https://doi.org/10.1029/2009JC005964>
- 960 Lübbecke, J.F., Brandt, P., Dengler, M., Kopte, R., Lüdke, J., Richter, I., Sena Martins, M.,
961 Tchikalanga, P.C.M., 2018. Causes and evolution of the southeastern tropical Atlantic
962 warm event in early 2016. *Clim. Dyn.* <https://doi.org/10.1007/s00382-018-4582-8>
- 963 Lutjeharms, J.R.E., Meeuwis, J.M., 1987. The extent and variability of South-East Atlantic
964 upwelling. *South Afr. J. Mar. Sci.* 5, 51–62.
965 <https://doi.org/10.2989/025776187784522621>
- 966 Lutz, K., Jacobeit, J., Rathmann, J., 2015. Atlantic warm and cold water events and impact on
967 African west coast precipitation. *Int. J. Climatol.* 35, 128–141.
968 <https://doi.org/10.1002/joc.3969>
- 969 Lutz, K., Rathmann, J., Jacobeit, J., 2013. Classification of warm and cold water events in the
970 eastern tropical Atlantic Ocean. *Atmospheric Sci. Lett.* 14, 102–106.
971 <https://doi.org/10.1002/asl2.424>
- 972 Marchesiello, P., McWilliams, J.C., Shchepetkin, A., 2001. Open boundary conditions for
973 long-term integration of regional oceanic models. *Ocean Model.* 3, 1–20.
974 [https://doi.org/10.1016/S1463-5003\(00\)00013-5](https://doi.org/10.1016/S1463-5003(00)00013-5)
- 975 McDougall, T.J., Barker, P.M., Marine, C., Research, A., 2011. Getting started with TEOS-
976 10 and the Gibbs Seawater (GSW) Oceanographic Toolbox : version 3.0, Version 3.0.
977 ed. Hobart, Tas. : CSIRO Marine and Atmospheric Research.
- 978 Mohrholz, V., Schmidt, M., Lutjeharms, J.R.E., 2001. The hydrography and dynamics of the
979 Angola-Benguela Frontal Zone and environment in April 1999 : BENEFIT Marine
980 Science. *South Afr. J. Sci.* 97, 199–208.
- 981 Moloney, C.L., Fennessy, S.T., Gibbons, M.J., Roychoudhury, A., Shillington, F.A., Heyden,
982 B.P. von der, Watermeyer, K., 2013. Reviewing evidence of marine ecosystem
983 change off South Africa. *Afr. J. Mar. Sci.* 35, 427–448.

984 <https://doi.org/10.2989/1814232X.2013.836135>

985 Monteiro, P.M.S., Dewitte, B., Scranton, M.I., Paulmier, A., Van der Plas, A., 2011. The role
986 of open ocean boundary forcing on seasonal to decadal-scale variability and long-term
987 change of natural shelf hypoxia. *Environ. Res. Lett.* 1–14.
988 <https://doi.org/10.1088/1748-9326/6/2/025002>

989 Monteiro, P.M.S., van der Plas, A.K., 2006. 5 Low oxygen water (LOW) variability in the
990 Benguela system: Key processes and forcing scales relevant to forecasting, in:
991 Shannon, V., Hempel, G., Malanotte-Rizzoli, P., Moloney, C., Woods, J. (Eds.),
992 Large Marine Ecosystems, Benguela Predicting a Large Marine Ecosystem. Elsevier,
993 pp. 71–90.

994 Monteiro, P.M.S., van der Plas, A.K., Mélice, J.-L., Florenchie, P., 2008. Interannual hypoxia
995 variability in a coastal upwelling system: Ocean–shelf exchange, climate and
996 ecosystem-state implications. *Deep Sea Res. Part Oceanogr. Res. Pap.* 55, 435–450.
997 <https://doi.org/10.1016/j.dsr.2007.12.010>

998 Moroshkin, K.V., Bunov, V.A., Bulatov, R.P., 1970. Water circulation in the eastern South
999 Atlantic Ocean. *Oceanology* 10, 27–34.

1000 Mosquera-Vásquez, K., Dewitte, B., Illig, S., 2014. The Central Pacific El Niño intraseasonal
1001 Kelvin wave. *J Geophys Res Oceans* 119, 6605–6621.
1002 <https://doi.org/10.1002/2014JC010044>

1003 Ostrowski, M., 2007. Impact of equatorial Kelvin waves on aggregations of sardinellas
1004 (*Sardinella* spp.) in Angolan waters. (Working paper). ICES.

1005 Ostrowski, M., da Silva, J.C.B., Bazik-Sangolay, B., 2009. The response of sound scatterers
1006 to El Niño- and La Niña-like oceanographic regimes in the southeastern Atlantic.
1007 *ICES J. Mar. Sci.* 66, 1063–1072. <https://doi.org/10.1093/icesjms/fsp102>

1008 Penven, P., Debreu, L., Marchesiello, P., McWilliams, J.C., 2006. Evaluation and application
1009 of the ROMS 1-way embedding procedure to the central california upwelling system.
1010 *Ocean Model.* 12, 157–187. <https://doi.org/10.1016/j.ocemod.2005.05.002>

1011 Picaut, J., 1983. Propagation of the Seasonal Upwelling in the Eastern Equatorial Atlantic. *J.*
1012 *Phys. Oceanogr.* 13, 18–37. [https://doi.org/10.1175/1520-](https://doi.org/10.1175/1520-0485(1983)013<0018:POTSUI>2.0.CO;2)
1013 [0485\(1983\)013<0018:POTSUI>2.0.CO;2](https://doi.org/10.1175/1520-0485(1983)013<0018:POTSUI>2.0.CO;2)

1014 Polo, I., Lazar, A., Rodriguez-Fonseca, B., Arnault, S., 2008. Oceanic Kelvin waves and
1015 tropical Atlantic intraseasonal variability: 1. Kelvin wave characterization. *J Geophys*
1016 *Res* 113, C07009. <https://doi.org/10.1029/2007JC004495>

1017 Quiñones, R.A., 2010. Eastern Boundary Current Systems, in: Liu, K.-K., Atkinson, L.,

1018 Quiñones, R., Talaue-McManus, L. (Eds.), Carbon and Nutrient Fluxes in Continental
1019 Margins: A Global Synthesis, Global Change – The IGBP Series. Springer Berlin
1020 Heidelberg, Berlin, Heidelberg, pp. 25–120. [https://doi.org/10.1007/978-3-540-](https://doi.org/10.1007/978-3-540-92735-8_2)
1021 [92735-8_2](https://doi.org/10.1007/978-3-540-92735-8_2)

1022 Richter, I., Behera, S.K., Masumoto, Y., Taguchi, B., Komori, N., Yamagata, T., 2010. On
1023 the triggering of Benguela Niños: Remote equatorial versus local influences. *Geophys*
1024 *Res Lett* 37, L20604. <https://doi.org/10.1029/2010GL044461>

1025 Rouault, M., 2012. Bi-annual intrusion of tropical water in the northern Benguela upwelling.
1026 *Geophys. Res. Lett.* 39. <https://doi.org/10.1029/2012GL052099>

1027 Rouault, M., Florenchie, P., Fauchereau, N., Reason, C.J.C., 2003. South East tropical
1028 Atlantic warm events and southern African rainfall. *Geophys Res Lett* 30, 8009.
1029 <https://doi.org/10.1029/2002GL014840>

1030 Rouault, M., Illig, S., Bartholomae, C., Reason, C.J.C., Bentamy, A., 2007. Propagation and
1031 origin of warm anomalies in the Angola Benguela upwelling system in 2001. *J. Mar.*
1032 *Syst.* 68, 473–488. <https://doi.org/10.1016/j.jmarsys.2006.11.010>

1033 Rouault, M., Illig, S., Lübbecke, J., Koungue, R.A.I., 2018. Origin, development and demise
1034 of the 2010–2011 Benguela Niño. *J. Mar. Syst., Benguela: Opportunity, Challenge*
1035 *and Change* 188, 39–48. <https://doi.org/10.1016/j.jmarsys.2017.07.007>

1036 Rouault, M., Servain, J., Reason, C.J.C., Bourlès, B., Rouault, M.J., Fauchereau, N., 2009.
1037 Extension of PIRATA in the tropical South-East Atlantic: an initial one-year
1038 experiment. *Afr. J. Mar. Sci.* 31, 63–71.
1039 <https://doi.org/10.2989/AJMS.2009.31.1.5.776>

1040 Shannon, L.V., Boyd, A.J., Brundrit, G.B., Taunton-Clark, J., 1986. On the existence of an El
1041 Niño-type phenomenon in the Benguela System. *J. Mar. Res.* 44, 495–520.
1042 <https://doi.org/10.1357/002224086788403105>

1043 Shannon, L.V., Nelson, G., 1996. The Benguela: Large Scale Features and Processes and
1044 System Variability, in: *The South Atlantic*. Springer Berlin Heidelberg, pp. 163–210.

1045 Shchepetkin, A.F., McWilliams, J.C., 2005. The regional oceanic modeling system (ROMS):
1046 a split-explicit, free-surface, topography-following-coordinate oceanic model. *Ocean*
1047 *Model.* 9, 347–404. <https://doi.org/10.1016/j.ocemod.2004.08.002>

1048 Shillington, F.A., 1998. The Benguela upwelling system off southwestern Africa, in: *The*
1049 *Global Coastal Ocean, Regional Studies and Syntheses, The Sea*. Wiley, New-York,
1050 pp. 583–604.

1051 Shillington, F.A., Reason, C.J.C., Duncombe Rae, C.M., Florenchie, P., Penven, P., 2006. 4

1052 Large scale physical variability of the Benguela Current Large Marine Ecosystem
1053 (BCLME), in: Shannon, V., Hempel, G., Malanotte-Rizzoli, P., Moloney, C., Woods,
1054 J. (Eds.), Large Marine Ecosystems, Benguela Predicting a Large Marine Ecosystem.
1055 Elsevier, pp. 49–70.

1056 Siegfried, L., Schmidt, M., Mohrholz, V., Pogrzeba, H., Nardini, P., Böttinger, M.,
1057 Scheuermann, G., 2019. The tropical-subtropical coupling in the Southeast Atlantic
1058 from the perspective of the northern Benguela upwelling system. PLOS ONE 14,
1059 e0210083. <https://doi.org/10.1371/journal.pone.0210083>

1060 Sowman, M., Cardoso, P., 2010. Small-scale fisheries and food security strategies in
1061 countries in the Benguela Current Large Marine Ecosystem (BCLME) region:
1062 Angola, Namibia and South Africa. Mar. Policy 34, 1163–1170.
1063 <https://doi.org/10.1016/j.marpol.2010.03.016>

1064 Strub, P.T., Shillington, F.A., James, C., Weeks, S.J., 1998. Satellite comparison of the
1065 seasonal circulation in the Benguela and California current systems. Afr. J. Mar. Sci.
1066 19.

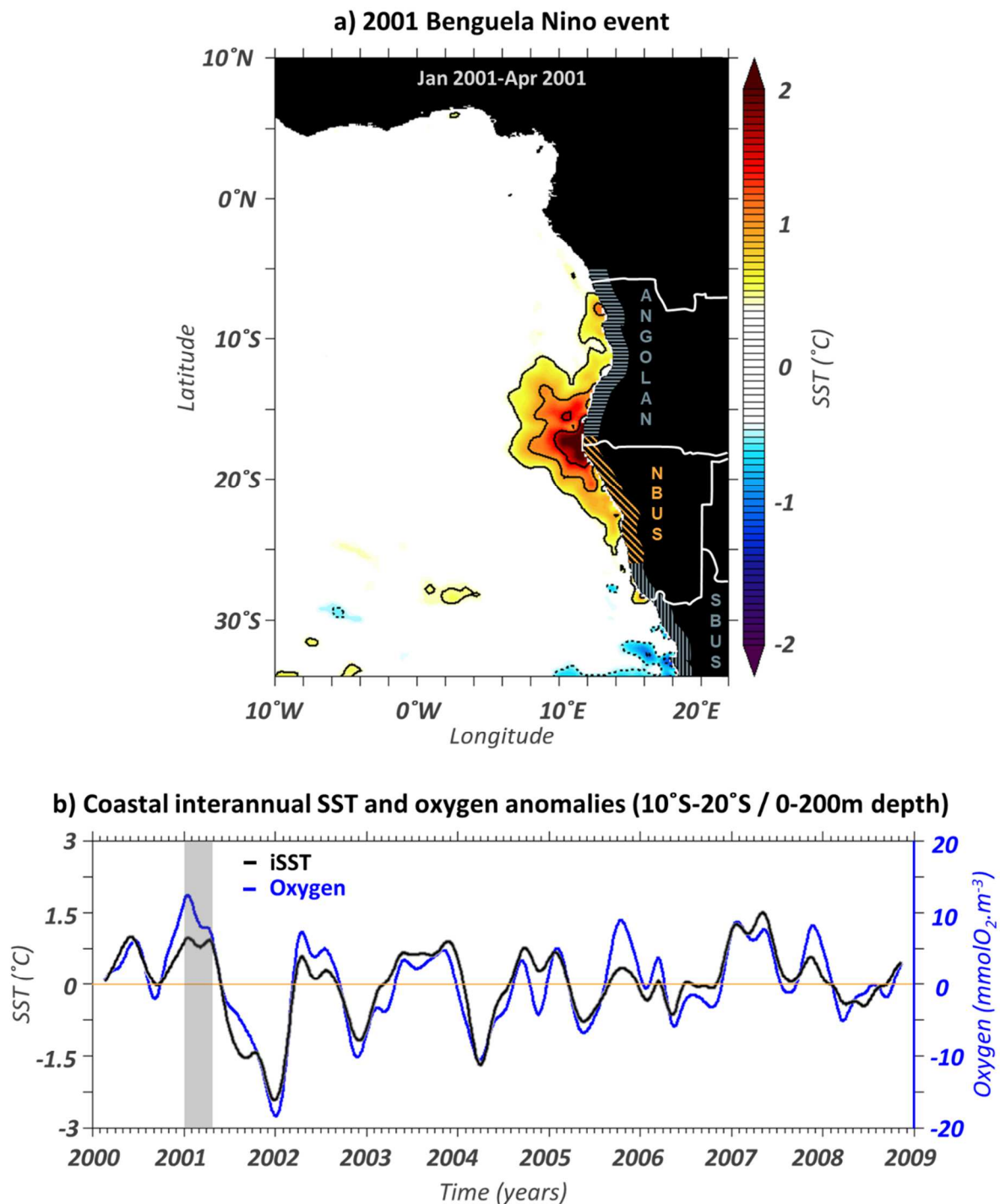
1067 Tchupalanga, P., Dengler, M., Brandt, P., Kopte, R., Macuéria, M., Coelho, P., Ostrowski, M.,
1068 Keenlyside, N.S., 2018. Eastern Boundary Circulation and Hydrography Off Angola:
1069 Building Angolan Oceanographic Capacities. Bull. Am. Meteorol. Soc. 99, 1589–
1070 1605. <https://doi.org/10.1175/BAMS-D-17-0197.1>

1071 van der Lingen, C.D., Shannon, L.J., Cury, P., Kreiner, A., Moloney, C.L., Roux, J.-P., Vaz-
1072 Velho, F., 2006. 8 Resource and ecosystem variability, including regime shifts, in the
1073 Benguela Current System, in: Shannon, V., Hempel, G., Malanotte-Rizzoli, P.,
1074 Moloney, C., Woods, J. (Eds.), Large Marine Ecosystems, Benguela. Elsevier, pp.
1075 147–184. [https://doi.org/10.1016/S1570-0461\(06\)80013-3](https://doi.org/10.1016/S1570-0461(06)80013-3)

1076 Woodhead, Hamukuaya, H., O’Toole, M.J., Stroemme, T., Kristmannsson, S., 1997a. Recruit
1077 mortalities in Cape hake, following exclusion from shelf habitat by persistent hypoxia
1078 in the Benguela Current, Namibia, in: Physical-Biological Interactions. Presented at
1079 the ICES International Symposium, Recruitment dynamics of exploited marine
1080 populations, pp. 26–27.

1081 Woodhead, Hamukuaya, H., O’Toole, M.J., Stroemme, T., Saetersdal, G., Reiss, M., 1997b.
1082 Catastrophic loss of two billion Cape hake recruits during widespread anoxia in the
1083 Benguela Current off Namibia, in: Physical-Biological Interaction. Presented at the
1084 ICES International Symposium, Recruitment dynamics of exploited marine
1085 populations, pp. 105–106.

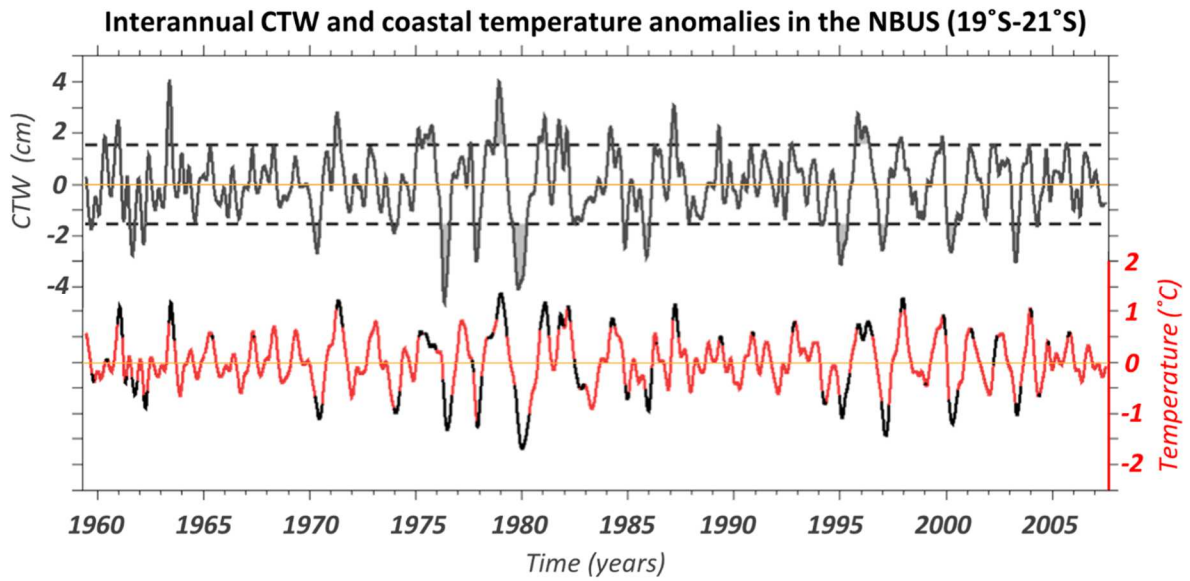
1086 Woodhead, P.M., Hamukuaya, H., O'Toole, M.J., McEnroe, M., 1998. Effects of oxygen
1087 depletion in shelf waters on hake populations off central and northern Namibia,
1088 International Symposium, Environmental variability in the South East Atlantic.
1089 NATMIRC, Namibia.
1090



1092

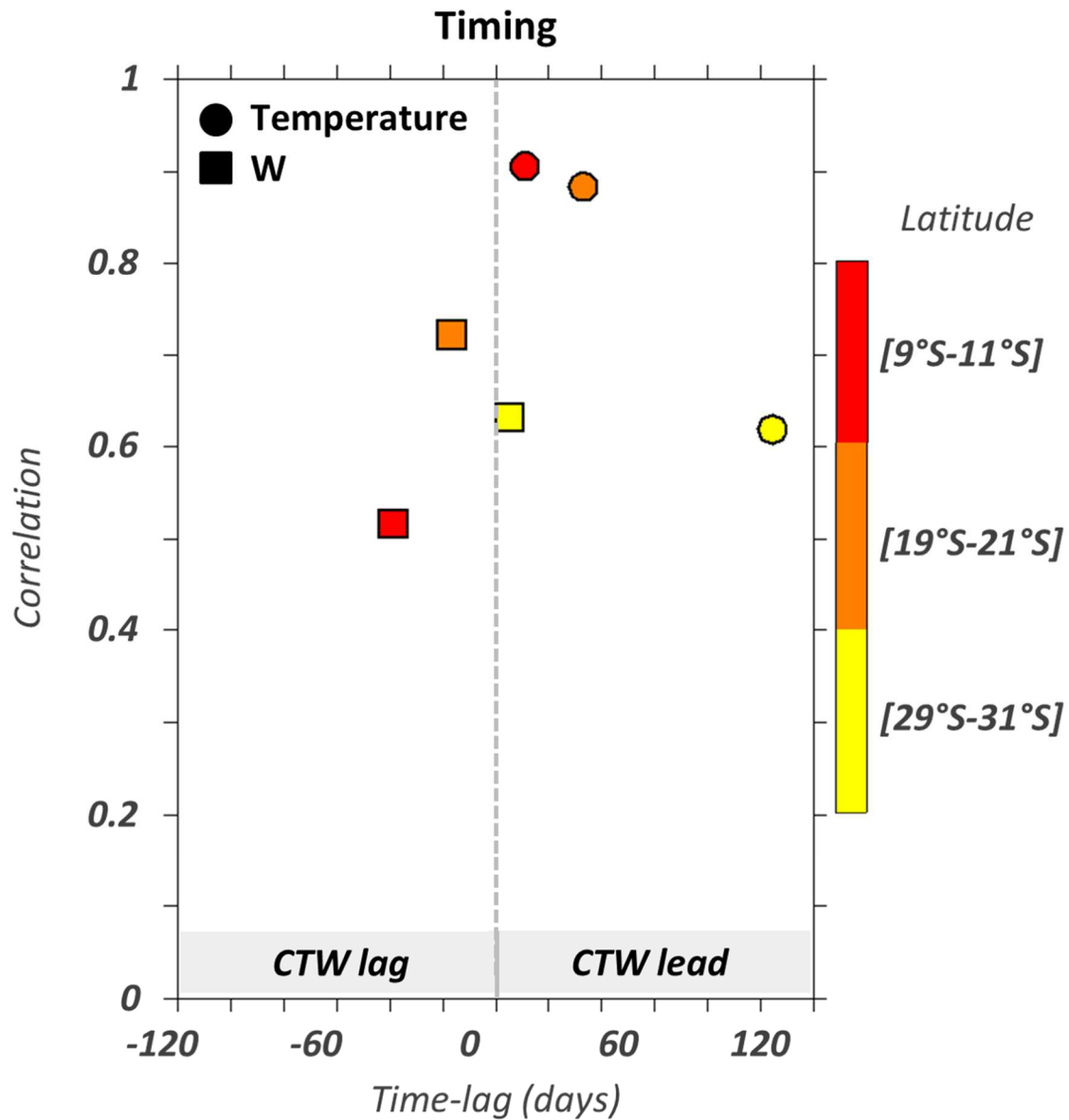
1093 **Figure 1:** a) Map of interannual Sea Surface Temperature (iSST; °C) from the GHRSSST
 1094 remotely-sensed observation (see the supporting information for more details about the data)
 1095 averaged during the peak phase of the 2001 Benguela Niño event (*cf.* grey vertical band in
 1096 **Fig. 1b**). Black contours interval is 0.5°C. White contours inland delineate the Angola,
 1097 Namibia and South Africa countries borders. The position of the three subsystems (Angolan,
 1098 NBUS and SBUS) is highlighted by the hatched lines in the African continent. b) Time series

1099 of iSST (black line; °C) and oxygen anomalies (averaged in the first 200m; blue line;
1100 mmolO₂.m⁻³) from the ROMS_{REF} simulation in Bachèlery et al. (2016). Model outputs have
1101 been averaged over a 0.5° coastal band from 10°S to 20°S.



1102

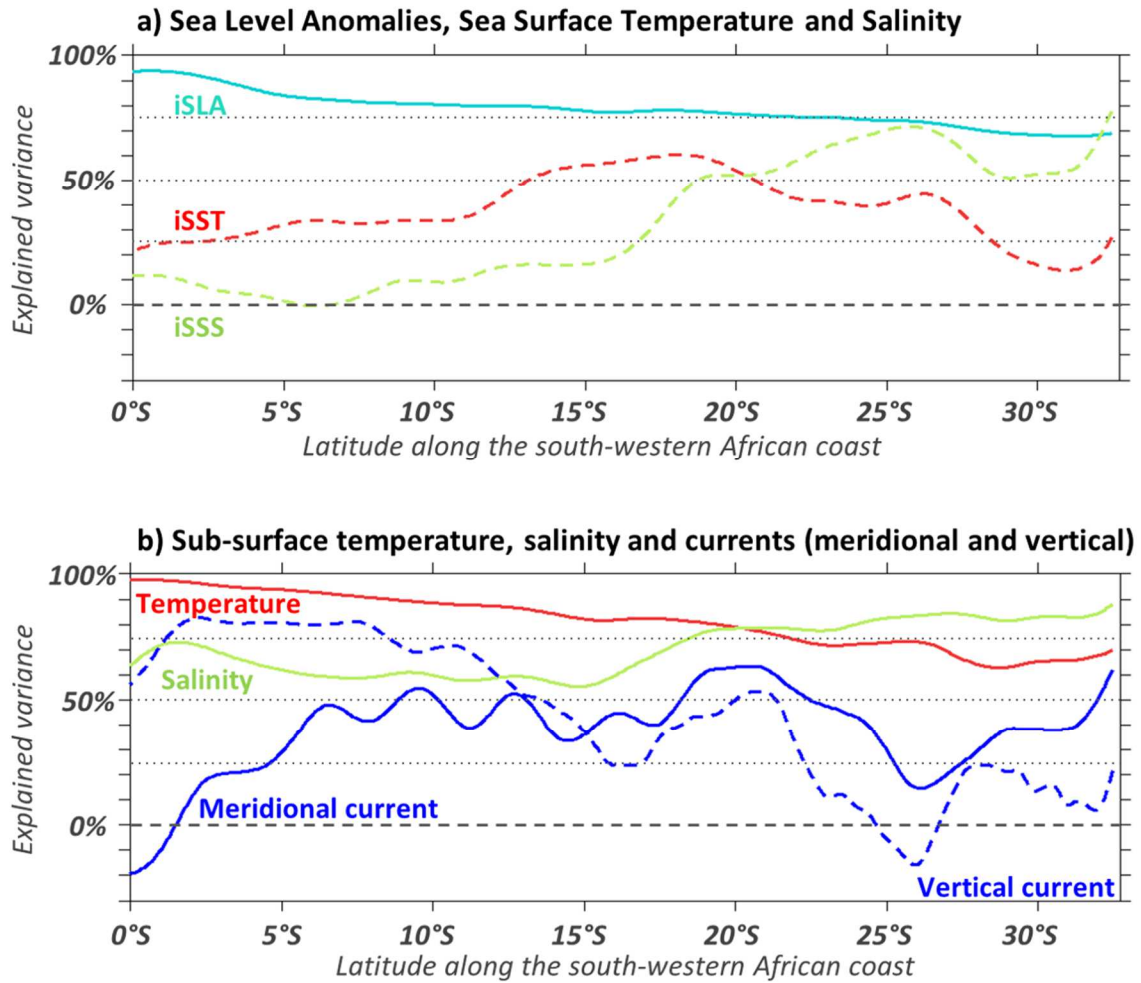
1103 **Figure 2:** Time series of ROMS-EQ interannual CTW123 (grey plain line; cm) and
 1104 temperature (within the first 200m; bottom red line; °C) anomalies averaged from 19°S to
 1105 21°S. Grey dashed lines and shading denote the position of ± 1.5 STD and the period of major
 1106 CTW123 events, respectively. The Peak phase of the selected CTW123 events (*cf.* grey
 1107 shading in the top time series) are reported with black lines on the bottom time series, shifted
 1108 by ~ 25 days with CTW123 leading in agreement with the timing found in **Figure 3** (red
 1109 circle).



1110

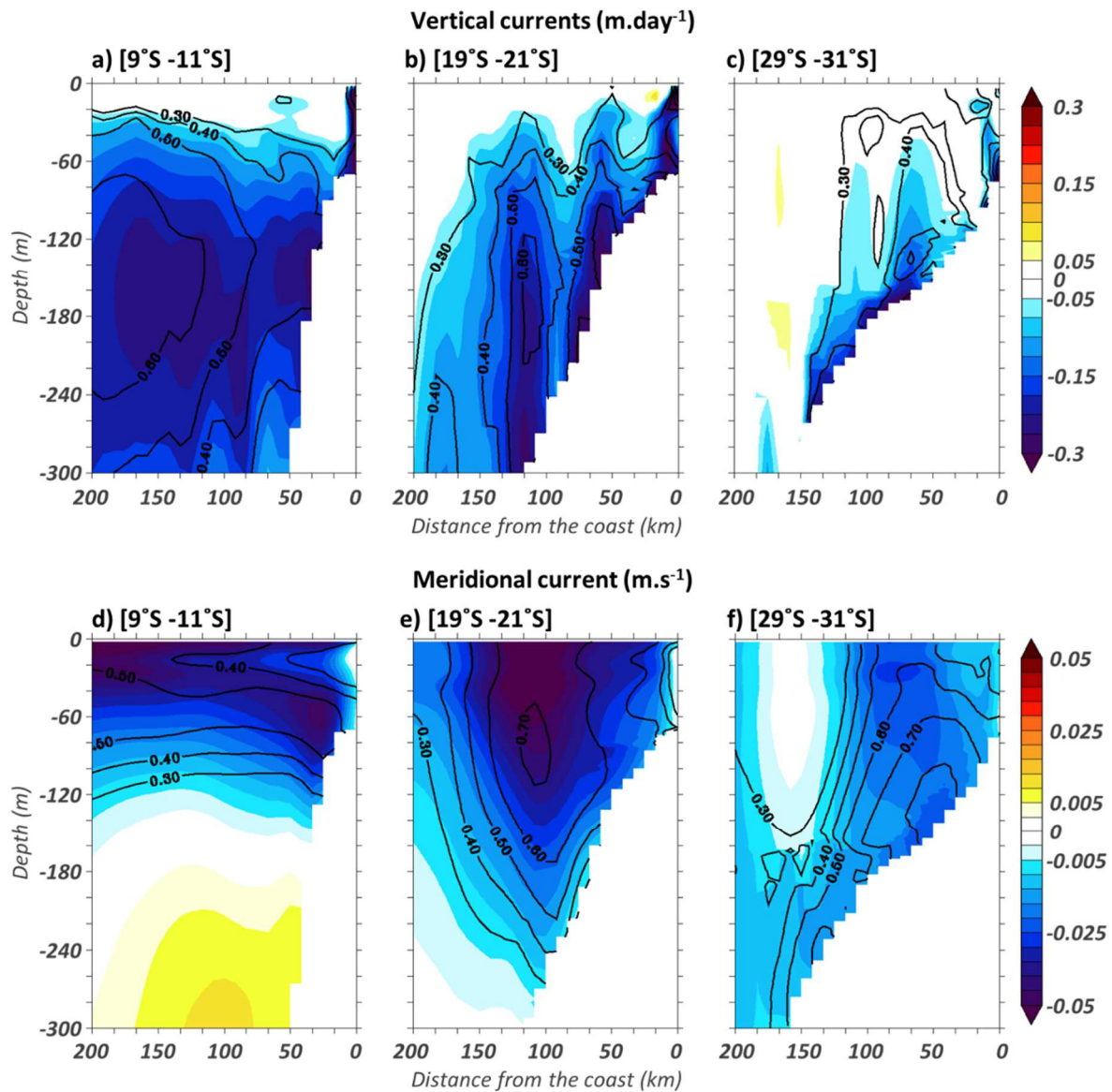
1111 **Figure 3:** Timing between the passage of ROMS-EQ interannual CTW and its signature on
 1112 the coastal ocean properties. Maximum lag-correlation between the interannual ROMS-EQ
 1113 CTW123 (Eq. 1) and the coastal (0.5°-width band) temperature (circles) and vertical current
 1114 (squares) anomalies averaged over the first 200m and within [9°S-11°S] (red), [19°S-21°S]
 1115 (orange) and [29°S-31°S] (yellow). Positive lags indicate that CTW leads.

Contribution of the remote forcing to the coastal interannual variability



1116

1117 **Figure 4:** Explained variance (in %, as defined by **Eq.2**) between ROMS-EQ and ROMS-CR
 1118 sensitivity experiments, averaged over the 0.5°-width coastal band along south-western
 1119 Africa. **a)** Interannual Sea Level Anomalies (iSLA; turquoise line), Sea Surface Temperature
 1120 (iSST; red dashed line) and Sea Surface Salinity (iSSS; green dashed line) anomalies. **b)**
 1121 Interannual temperature (red line), Salinity (green line), meridional (blue line) and vertical
 1122 (blue dashed line) currents anomalies averaged over the first 200 meters.



1124

1125 **Figure 5:** Composite cross-shore sections at 9°S-11°S (left panels), 19°S-21°S (middle1126 panels) and 29°S-31°S (right panels) of ROMS-EQ interannual vertical (top panels; m.day⁻¹)1127 and meridional (bottom panels; m.s⁻¹) currents anomalies averaged during periods of1128 energetic CTW events (*cf.* grey shading in **Figure 2a**). See **section 2.6** for details on the

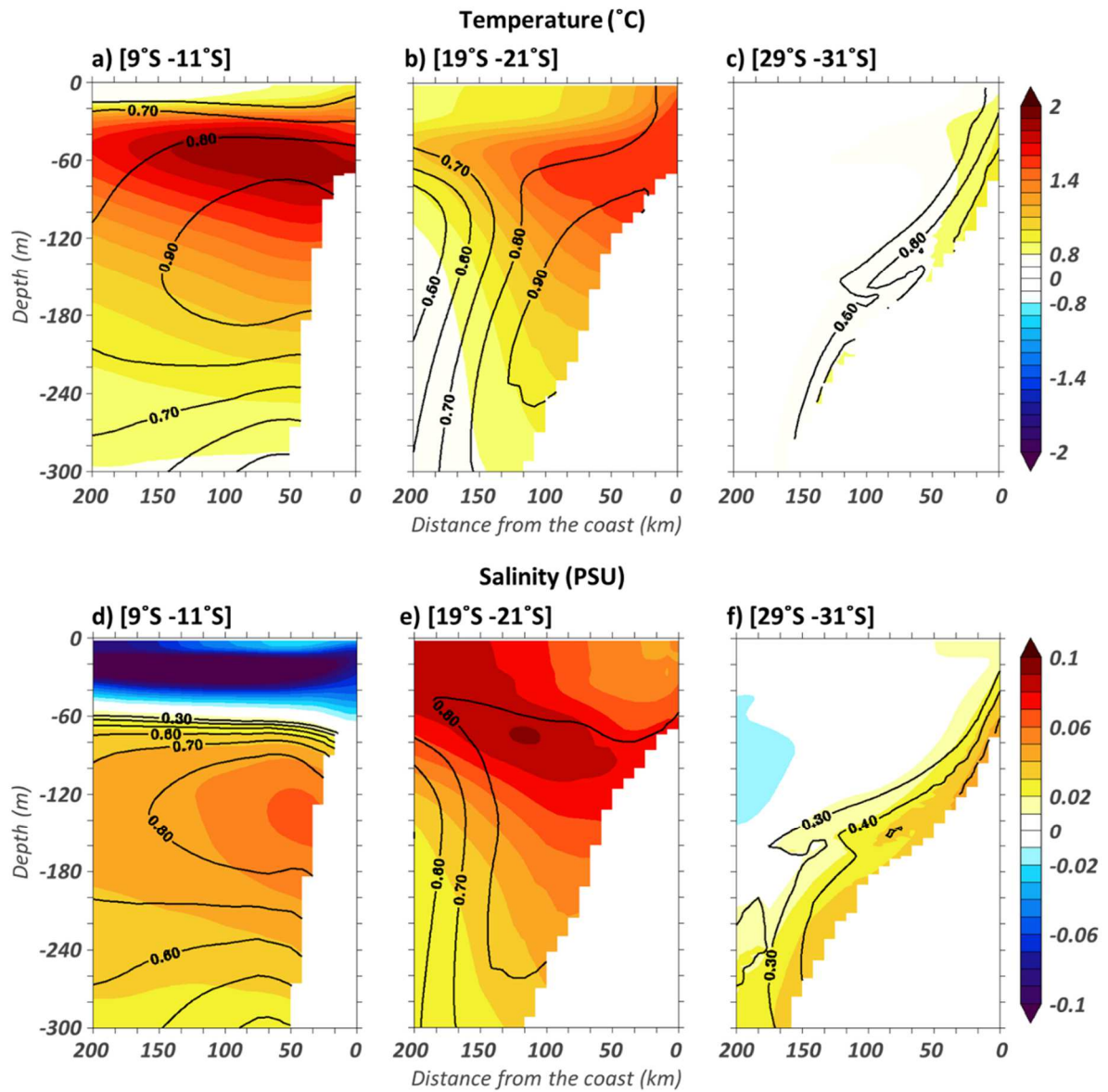
1129 compositing technique. Contours show correlation (1958-2008) between the interannual

1130 current variability and CTW123 indexes shifted in time by the corresponding lag obtained in

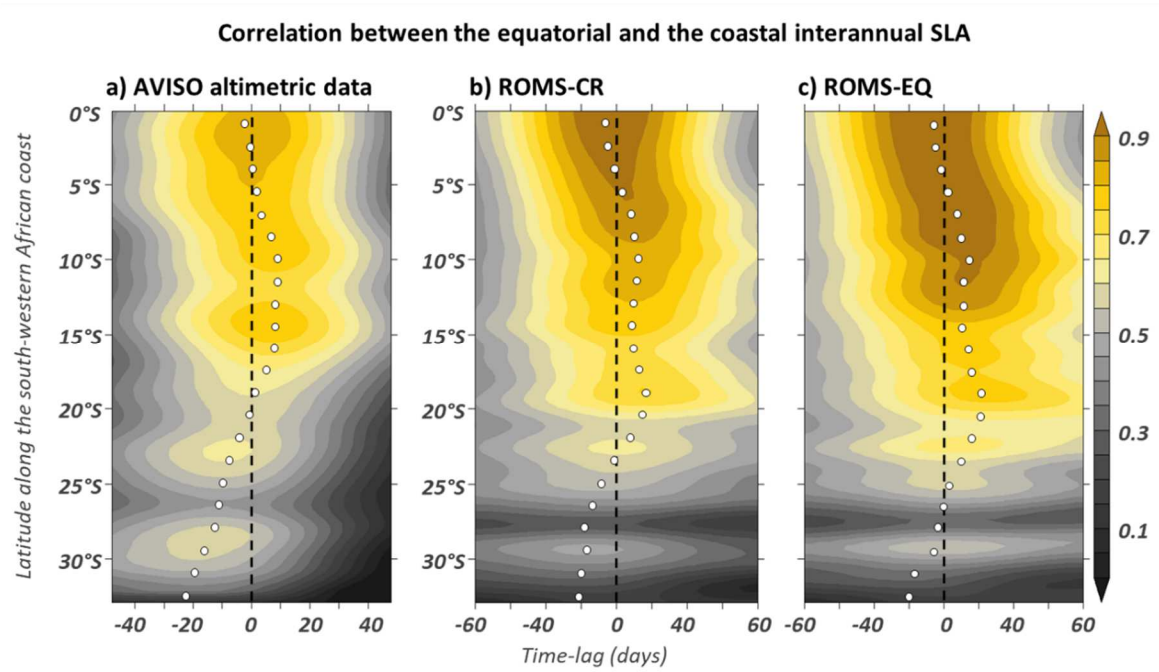
1131 **Figure 3.**

1132

1133

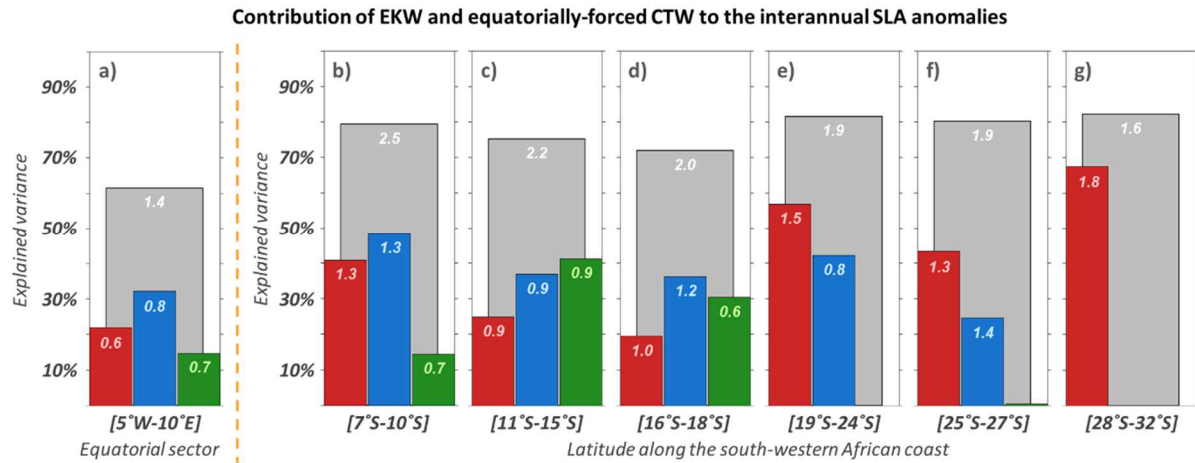


1134
 1135 **Figure 6:** Same as **Figure 5** for temperature (top panels; °C) and salinity (bottom panels;
 1136 PSU) interannual anomalies.
 1137



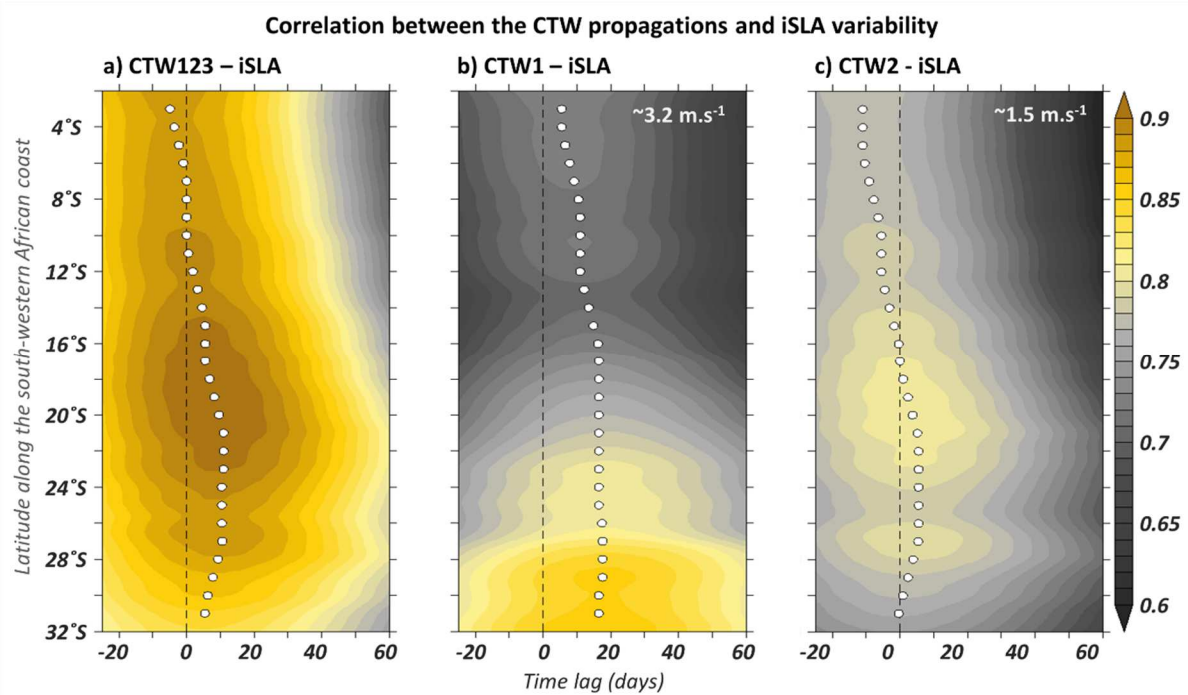
1138

1139 **Figure 7:** Lag-correlation between interannual Sea Level Anomalies averaged within [5°W-
 1140 5°E; 1°S-1°N] and over 1°-width coastal band as a function of the latitude and lag (days).
 1141 Positive lags correspond to the equatorial variability leading. White dots highlight the timing
 1142 of the maximum correlation in function of latitude (every 1.5°). **a)** Remotely-sensed Aviso
 1143 observations. **b)** ROMS-CR and **c)** ROMS-EQ model solutions.



1144

1145 **Figure 8:** a) Bar-charts quantify the explained variance (in %; Eq. 2) of the interannual
 1146 SODA EKW mode 1 (red), 2 (blue), 3 (green) and their summed-up contribution (grey) to the
 1147 equatorial (5°W-10°E / 1°N-1°S) interannual Sea Level Anomalies (iSLA) of ROMS-EQ.
 1148 Values on the top bar give the variance (cm²) of each mode. b-g) Same as panel a) for the
 1149 ROMS-EQ CTW contributions to the coastal (in a 0.5° width band) iSLA averaged within b)
 1150 [11°S-15°S], c) [16°S-18°S], d) [19°S-24°S], e) [25°S-27°S] and, f) [28°S-32°S].



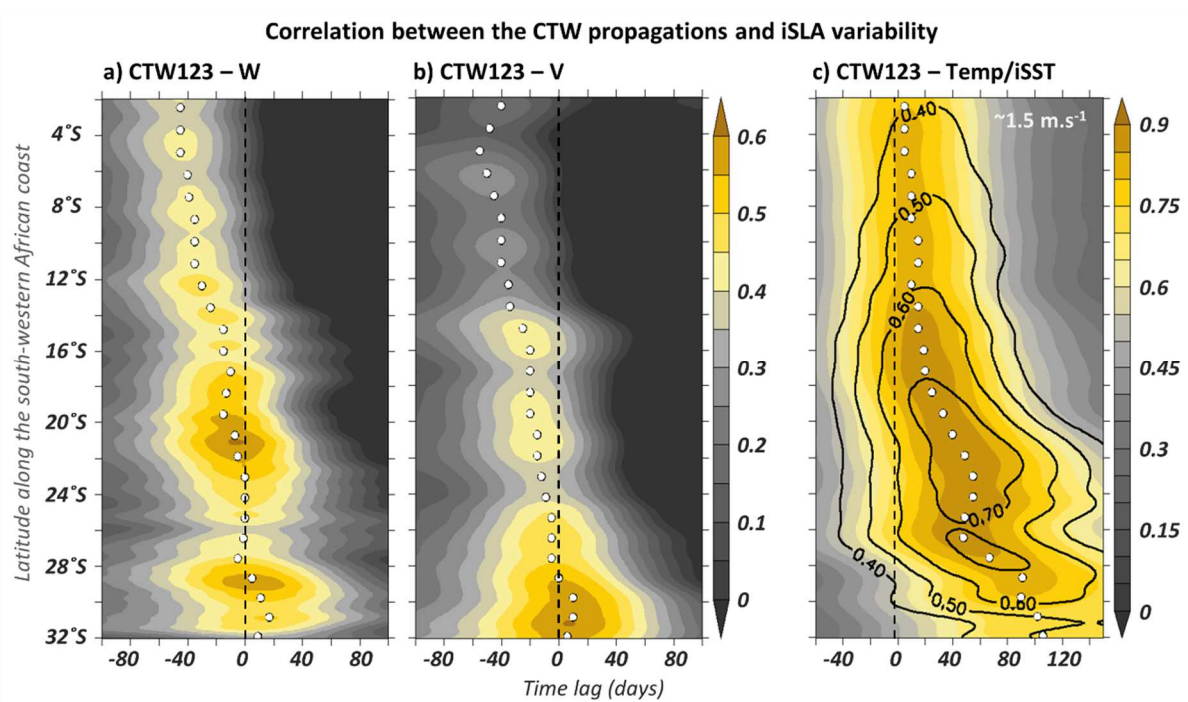
1151
 1152 **Figure 9:** Lag-correlation between interannual ROMS-EQ CTW signal ((a) summed-up
 1153 contribution of mode 1, 2 and 3; (b) mode 1; (c) mode 2 averaged within [7°S-9°S - 0.5°
 1154 coastal band] and the interannual Sea Level Anomalies as a function of latitude along the
 1155 south-western coast of Africa and time lag (days). Positive lags stand for the CTW signal
 1156 leading. White dots denote the timing of the maximum correlation in function of latitude
 1157 (every 1°). Values listed in the right upper corner (in white) correspond to the modal CTW
 1158 phase speed (m.s^{-1}) estimated based on the slope of least-squares best-fit straight lines passing
 1159 through the maximum correlations (white dots) within [4°S-32°S], and [4°S-22°S] for panel
 1160 b) and c) respectively.

1161

1162

1163

1164



1165

1166 **Figure 10:** Lag-correlation between the ROMS-EQ interannual CTW123 signal (averaged

1167 within 7°S-9°S - 0.5° coastal band) and interannual (a) vertical current, (b) meridional

1168 current, (c) temperature and Sea surface temperature (contours) anomalies as a function of

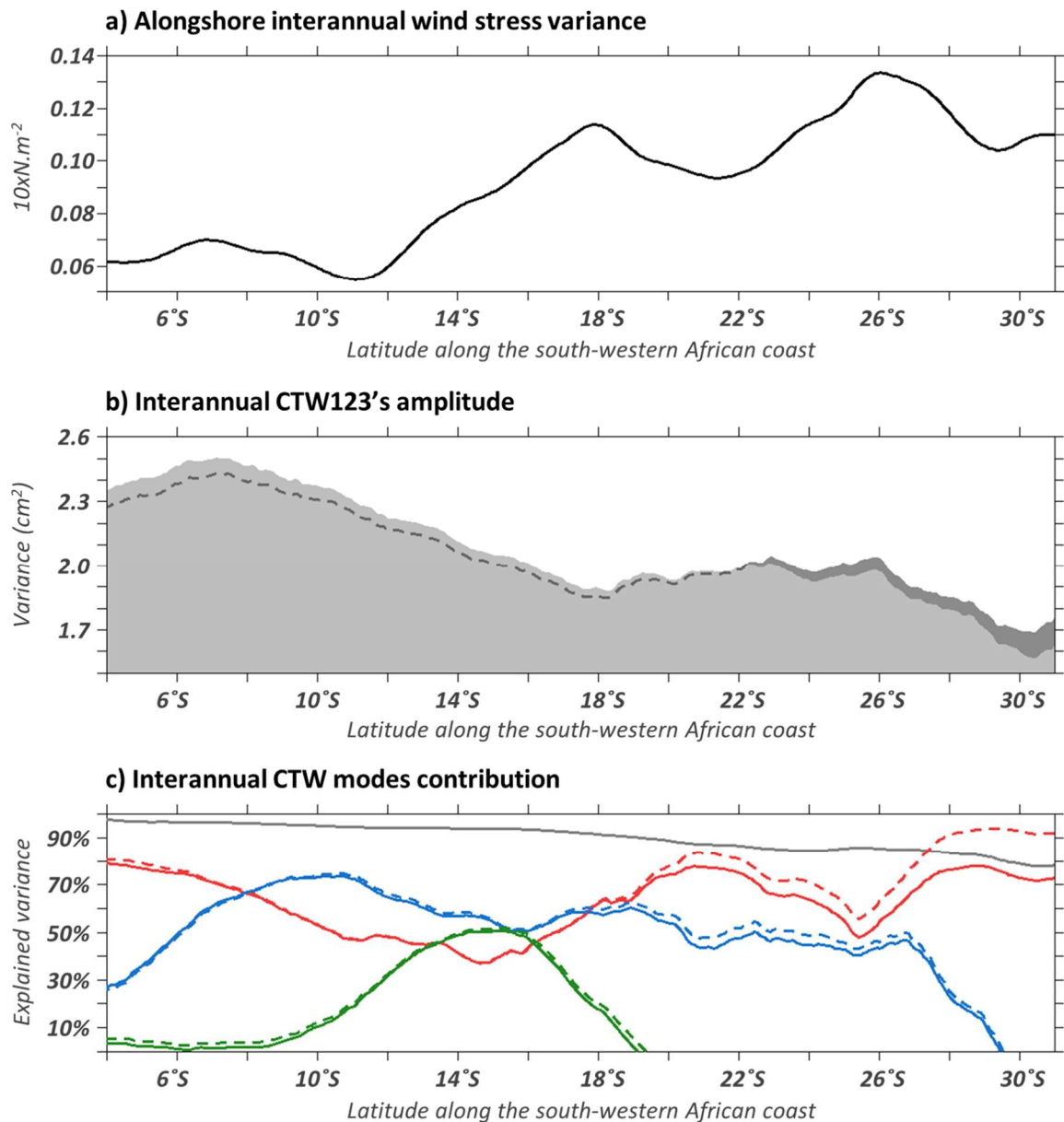
1169 latitude along the south-western coast of Africa and time lag (days). Positive lags stand for

1170 the CTW signal leading. White dots denote the timing of the maximum correlation in

1171 function of latitude (every 1°). The temperature and currents variable have been averaged

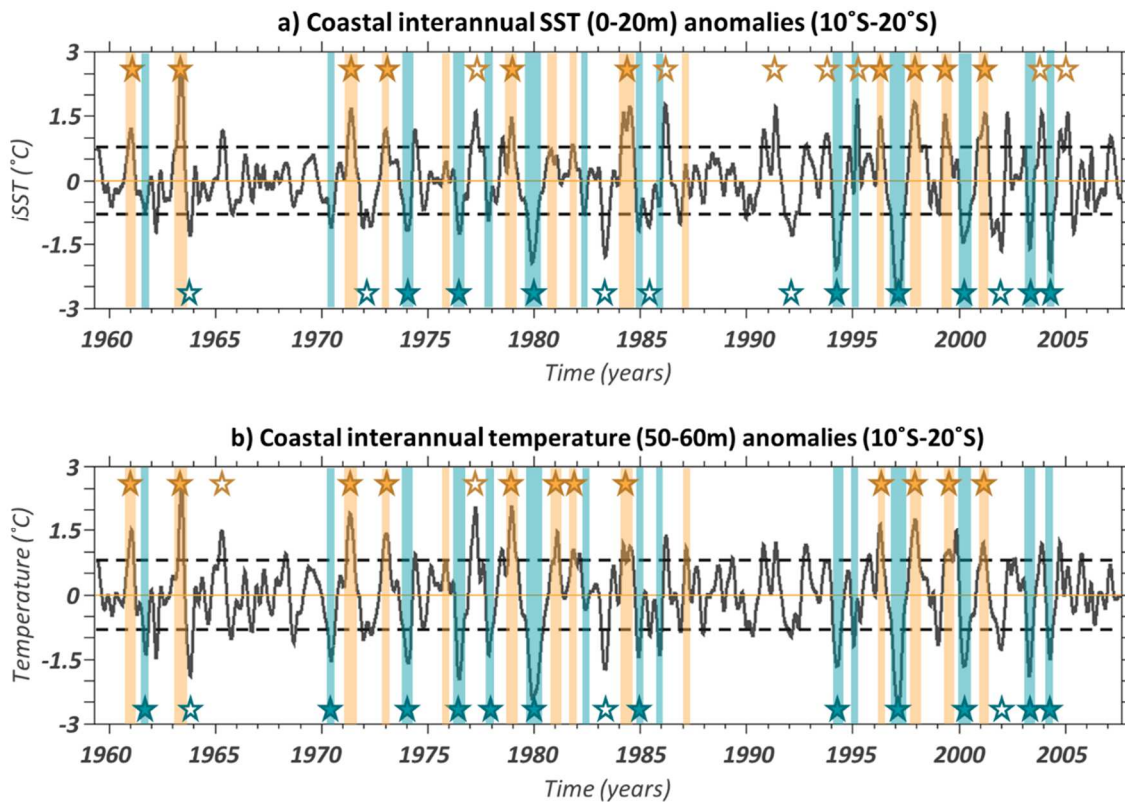
1172 over the first 200m depth within a 1° coastal band.

1173



1175

1176 **Figure 11:** a) Variance of the interannual alongshore wind stress anomalies ($10 \times N \cdot m^{-2}$) as a
 1177 function of latitude along the south-western coast of the African continent using ROMS-CR
 1178 outputs. Wind data have been averaged in a 2° -width coastal band. **b-c)** Mean (1958-2008)
 1179 interannual CTW characteristics averaged over a 0.5° width coastal band. **b)** Variance of the
 1180 summed-up contribution of the three gravest CTW modes (CTW123; **Eq. 1**) to SLA (cm) in
 1181 function of latitude along the south-western African coast. Dark and pale grey show the
 1182 results for the ROMS-CR and ROMS-EQ, respectively. **c)** Plain red, blue, green and grey
 1183 lines count for the explained variance (in %; *cf.* **Eq. 2**) of ROMS-EQ CTW modes 1, 2, 3 and
 1184 their summed-up contribution relative to ROMS-CR CTW123. Dash lines show the same
 1185 quantification for ROMS-CR.



1186

1187 **Figure 12:** a) 0-20 m depth interannual Sea Surface Temperature (iSST; °C) anomalies
 1188 averaged from 10°S to 20°S in an 1° coastal fringe of ROMS-CR. Extreme downwelling and
 1189 upwelling ROMS-CR CTW123 propagating episodes (*cf.* section 2.6 for more details on the
 1190 threshold) are emphasized with the yellow and turquoise vertical bars, respectively. Yellow
 1191 (turquoise) stars denote the extreme Benguela Niño (Niña) episodes defined as interannual
 1192 anomalies larger than ± 1 STD (grey dashed lines) for at least 3 months. Extreme Benguela
 1193 Niño (Niña) that do not coincide with an extreme downwelling (upwelling) CTW event are
 1194 depicted by a red (blue) star. b) Same as **Figure 12a** for interannual temperature anomalies
 1195 averaged under the mixed layer between 50-60 m depth.